MOFs functionalization of 3D printed mullite complex architectures for CO2 capture

Applied Materials Today 40 (2024) 102407

Contents lists available at ScienceDirect

Applied Materials Today

journal homepage: www.elsevier.com/locate/apmt

MOFs functionalization of 3D printed mullite complex architectures for CO_2 capture

Arianna Bertero [a], Julien Schmitt [b], Helena Kaper [b], Bartolomeo Coppola [a], Paola Palmero [a], Jean-Marc Tulliani [a,*]

[a] Politecnico di Torino, Department of Applied Science and Technology, INSTM R.U. Lince Laboratory, Corso Duca Degli Abruzzi 24, Torino, Italy
[b] Saint-Gobain Research Provence, 550 Rue Alphonse Jauffret, Cavaillon, France

ARTICLE INFO

Keywords:
Digital light processing
CO_2 capture
Mullite
Porous ceramics
Triply periodic minimal surface
Metal organic frameworks

ABSTRACT

Anthropogenic emissions of green-house gases and increasing CO_2 atmospheric concentration are considered the major causes of global warming and ocean acidification. Carbon capture and sequestration turned out to be a valuable strategy to help mitigating these problems, making it urgent to develop novel materials able to selectively capture CO_2. Thus, in the present experimental study, a new system for CO_2 capture based on porous mullite ($3Al_2O_3{\cdot}2SiO_2$) substrates fabricated by Digital Light Processing and properly functionalized with Metal Organic Frameworks (MOFs) was developed. Printable ceramic pastes were obtained by mixing in proper amounts commercial mullite powders to a photocurable commercial resin with a dispersant and a sintering additive to optimize the rheological behaviour, printability, and solid loading. Then, different geometries were successfully shaped with high accuracy: bars, pellets, as well as monoliths with two structures, grid-like and Schwartz primitive triply periodic minimal surface (TPMS).

After debinding and sintering of the samples, mullite substrates were successfully functionalized with HKUST-1 ($Cu_3(BTC)_2$) crystals by a two-step solvothermal synthesis process. HKUST-1 powders, as well as blank and coated lattice monoliths were tested in a catalytic bench reactor under 1% CO_2 flux (99% He). Before each measurement samples were heated at 120 °C for 4 h under He flux for regeneration. The samples showed an efficient CO_2 adsorption capacity, and the regeneration efficiency led to reusable and durable systems. Preliminary results showed that the TPMS structure was a more efficient substrate than grid-like architecture for capturing CO_2, because of its higher surface area. Thus, this study demonstrates how the combination between additive manufacturing and MOFs technologies can set the stage to produce efficient engineered systems for CO_2 capture.

1. Introduction

Climate change is one the most severe threats of the 21st century and is strongly influenced by human activities. Greenhouse gases release, e.g. carbon dioxide (CO_2) and methane (CH_4), are univocally recognized to be the main responsible for global warming. Comparing to the pre-industrial era, CO_2 atmospheric concentration almost doubled reaching 422 parts per million (ppm) in December 2023 [1,2]. This resulted in a temperature rise of 1.2 °C in the first decade of the 21st century compared to the global temperature in 1850–1900 [3]. This situation, if left uncontrolled, can result in severe damages to the environment and human populations. Hence, during Paris Agreement of 2021, governments set the target to limit the global temperature increase below 1.5 °C. To reach the ambitious goal, Europe targets at being the first continent reaching net zero or negative CO_2 emissions by 2030 [4]: this requires an immediate and significant greenhouse gases reduction [1–4]. To achieve this challenging target, several mitigation options have been proposed (e.g. transition to renewable energies, electrification of the energy demand etc. [3]). Among them, carbon capture, utilisation, and storage may account for up to 15% of the cumulative reduction in emissions according to the Sustainable Development Scenario [5]. Current materials for Carbon Capture and Sequestration (CCS) involve amine solvents, ionic liquids, membranes and porous materials. In particular, amine chemical absorption is a common solution employed at the industrial scale. But, despite the high CO_2 capture efficiency, chemical absorption evidence dramatic drawbacks: a need for

* Corresponding author.
E-mail address: jeanmarc.tulliani@polito.it (J.-M. Tulliani).

https://doi.org/10.1016/j.apmt.2024.102407
Received 9 April 2024; Received in revised form 4 August 2024; Accepted 22 August 2024
Available online 2 September 2024

high absorber amounts, large energy consumption and low corrosion resistance [6]. Thus, a faster transition to net zero emission increases the need for novel solid adsorbents able to selectively capture CO_2. So far, several classes of porous materials have been intensively studied and Metal Organic Frameworks (MOFs) attracted increasing attention due to their unique pore characteristic and interconnected network. MOFs seem preferable to the well-known zeolites and activated carbons, due to a higher CO_2 uptake capacity, more effective regeneration processes and better selectivity especially in the system N_2/CO_2 [6,7]: in fact, they have shown a great potential for CCS applications [2,3,6–8]. These promising hybrid materials are formed by two main building blocks, organic molecules, and metal-based nodes. The organic part usually consists of coordination polymers based on bi- to tetravalent carboxylic acids, acting as bridging ligands through a specific functional group (e.g. carboxylate, pyridyl), coordinated to metal ions or metal oxide clusters (e.g., Al^{3+}, $Cr^{3+,}$ Cu^{2+}, or Zn^{2+}). These crystalline systems have a microporous structure characterized by a specific surface area up to 6, 000 m^2g^{-1}, high porosity volume (reaching 90%) and low density (from 0.21 to 1.00 $g.cm^{-3}$), as well as high thermal and chemical stability [6–8]. For these reasons, they show a great potential for various applications such as gas sensors [9–11] catalysts [12–14] electric conductors [15–18] or in biomedicine [19–21]. Among them, the use of HKUST-1 for CCS has been reported by several authors [22–25]. HKUST-1 ($Cu_3(BTC)_2$), also known as MOF-199 or Cu-BTC, consists of copper nodes (Cu^{2+}) and benzene-1,3,5-tricarboxylate (BTC): each metal centre is coordinated with four oxygen atoms and water molecules[23,26,27]. The electrically neutral and face-centred crystalline framework of HKUST-1 provides superior thermal stability, good functionalization potential and high specific surface area (up to 2,000 m^2/g [8,28–35]), which are typically desired properties for gas separation and adsorption applications. Despite its well-known drawback of instability in humid environment [32,40], HKUST-1 has a promising CO_2 capture ability, relying on the combination of two different mechanisms [8,23,28–30, 32–38]. First, its microporous 3D-channels network provides a molecular sieving effect. It contains a bimodal pore size distribution displaying larger cages with 0.9 nm diameter that coexist with smaller pores of 0.35 nm diameter. The smaller micropores act as molecular sieves towards CO_2. Indeed, the kinetic diameter of CO_2 is 0.33 nm, and it can pass through HKUST-1 network, while bigger molecules, such as CH_4 and N_2 with kinetic diameters of 0.38 and 0.364 nm respectively, are too large to enter the small pores [39]. Second, HKUST-1 can selectively adsorb CO_2 molecules due to the presence of Cu active sites. In HKUST-1 paddlewheel structure, water molecule in axial position can be thermally removed from the copper node, making them able to interact with the CO_2 quadrupole moment [40]. Nevertheless, a direct use of MOFs in the adsorption separation process has severe limitations related to the use of powder bed systems, because of bad manageability, high pressure drops, low mass transfer rate, and poor recyclability [41]. Recent works are focusing on producing self-standing monoliths of adsorbent materials (such as MOF) that consist in a mixture of the adsorbent powder with a suitable binder and additives using additive manufacturing, mainly Direct Ink Writing [42–46]. Despite large MOFs or zeolites weight fractions (>80 wt%), the employment of a polymeric binder allows for a weak structural support only, while blocking the access to the micro or mesoporous network of the adsorbent powder [43,53]. For example, the shaping of HKUST-1 (60 wt%) with Torlon as binder induced a reduction of its specific surface area from 830 to 290 $m^2.g^{-1}$ and of its pore volume from 0.43 to 0.17 cm^3/g [42]. A calcination/sintering step after shaping hence allows removing the organic binder while strengthening the material. Zeolites such as zeolite 13X were successfully prepared via this approach, exhibiting remarkable CO_2 sorption properties (up to 50 mg/g of CO_2 adsorbed as evidenced by TGA measurements) [46]. Nonetheless, using a similar route to shape MOFs on ceramic substrates such as HKUST-1 remains challenging as their degradation temperature is lower than the one used for binder removal and substrate sintering [47]. A valuable strategy to overcome these issues is the incorporation of microporous materials [48,49], into pre-shaped substrates to obtain various composites, combining the advantageous textural properties of the coating with the hierarchical porous supports. Production of activated structural supports is still challenging: even if several investigations have been carried out on the deposition of microporous materials, such as MOFs [50–56] and zeolites [57–62] on different substrates, various drawbacks are still unsolved. Main crucial limitations concern the complexity of the preparation and functionalization of the macroporous scaffolds, low crystals loading, weak mechanical stability and adhesion of MOF films, but also low adsorption capacity compared to the powder counterparts. Growing MOF crystals on the walls of monolithic supports have been shown as a facile approach to shape this commonly studied class of adsorbent [50,51,53,54,57,59,61,63–69]. Specifically, HKUST-1 coatings have been manufactured on alumina substrates in the shape of granules [68] or porous foams [69] which were functionalized with fairly high MOF loadings (4.5, 6.0, 12.7 wt%) modifying the synthesis temperature. These coating strategies were not applied to structured supports with controlled microporosity. Thus, the current study is proposing to combine the CO_2 adsorption properties of HKUST-1 with the efficient design and support offered by a ceramic substrate realized by Digital Light Processing (DLP), an additive manufacturing method. Due to their chemical and thermal stability, porous ceramics show a great promise in environmental applications and recently attracted the attention of the scientific community as suitable growth substrates, providing desirable advantages, such as structural lightweight, good thermal conductivity and mass transport properties [70,71]. For these reasons, several studies explored various complex porous structures, especially Triply Periodic Minimal Surfaces (TPMS), tailoring their anisotropic morphologies, pore-size and pore connectivity to optimize the systems performance [72–81]. Among all the techniques to fabricate porous ceramics, additive manufacturing leads to an accurate production of geometrically complex and interconnected substrates [82–84]. In particular, DLP stands out for its high resolution and dimensional accuracy in realizing customized tiny complex geometries with superior surface quality [85–89] . In the wide world of ceramics, mullite ($3Al_2O_3{\cdot}2SiO_2$) is an ideal refractory material to produce porous scaffolds due to its durability, high mechanical strength, creep resistance, low thermal expansion, and high thermal shock resistance [90–93]. In addition, it has been demonstrated that mullite structures with complex design, tailored porosity and permeability can be shaped by DLP technique [94–99]. Continuous and resistant HKUST-1 coatings were produced on the mullite substrates and results show that this design induces an increase of the CO_2 capture properties of the monoliths in respect to the MOFs powder bed. In fact, several characterizations were conducted to study the 3D-printed monoliths, HKUST-1 powder, and their mutual interaction. Finally, preliminary CO_2 adsorption tests allow evaluating their applicability for CCS aim. The synergic combination of the macroporous ceramic scaffold and MOFs microporosity led to the innovative development of a hierarchically-structured efficient CO_2 capture system.

2. Experimental

2.1. Fabrication of ceramic substrates

2.1.1. Mullite powder characterization

Commercial mullite powder ($3Al_2O_3{\cdot}2SiO_2$) supplied by Baikowski SAS (SA 193CR, Poisy, France) was used to fabricate the ceramic substrates. The particle size and granulometric distribution was checked by laser granulometry (Mastersizer 3000, Malvern Pan'alytical, Worcestershire, UK). The morphology of the powder was characterized by means of a Field Emission Scanning Electron Microscope (FESEM, Hitachi S4000, Tokyo, Japan).

The sinterability was investigated by dilatometric analysis (Netzsch Geraetebau GmbH 402E, Selb, Germany), performed on pressed bars, up to 1,550 °C, at the heating rate of 10 °C/min. Magnesium nitrate

hexahydrate ($Mg(NO_3)_2{\cdot}6H_2O$ supplied by Sigma-Aldrich, 99.0% purity, Milan, Italy) was used as a sintering aid, in the required amount to yield 1 wt% of MgO during sintering. This was done to improve the density of the sintered mullite [100]. Magnesium nitrate was mixed with the mullite powder, in water medium, and the mixture was then dried and uniaxially-pressed.

Pressed ceramic sintered bodies were characterized by mercury intrusion porosimetry (MIP, Micormeritics Autopore V by Micromeritics Instrument Corporation, Norcross, GA, USA). Two measurements were done for each sintering temperature (1,450 °C and 1,550 °C).

The phase composition of the powder and sintered samples was determined by X-Ray Diffraction (XRD, Malvern Pan'alytical, Worcestershire, UK) with a CuKα radiation source (0.154056 nm) in the 2θ range 5–70° A time per step of 22.95 s and step size of 0.0066° were used.

2.1.2. Mullite slurry elaboration

Mullite slurry for 3D printing was prepared starting from a photocurable commercial resin (Admatec Europe BV, Alkmaar, The Netherlands), which consists of acrylates-based monomers containing the photoinitiator (diphenyl(2,4,6-trimethylbenzoyl) phosphine oxide). A commercial dispersant (Disperbyk-103, BYK Chemie, Wesel, Germany) was used to improve the stability of mullite powder in the resin and hence enhance the solid loading in the slurry.

The ceramic slurry was prepared by mixing the liquid monomer with the dispersant (the amount of dispersant corresponds to 5.0 wt% with respect to the dry mullite powder) under mechanical stirring for 15 min. Then, mullite powder was gradually added to the mixture under stirring in order to obtain a final solid loading of 69 wt%. Finally, magnesium nitrate hexahydrate was added, and the slurry mixed again. The total mixing process lasted 45 min. The obtained slurry was milled in agate jars with agate spheres (d = 10 mm) for 6 h at 350 rpm in a planetary miller (Fritsch Pulverisette, Fritsch GmbH, Idar-Oberstein, Germany). The slurry was then degassed for 30 min under vacuum by means of a rotary pump, in order to release the entrapped air bubbles.

The rheology of the slurry was investigated using a rotational rheometer (Kinexus Pro+, Netzsch Gerätebau GmbH, Selb, Germany) equipped with stainless steel parallel plates (20 mm diameter), with a 1 mm gap between plates, and by applying shear rates of 0.1–1,000s^{-1} at 25 °C.

2.1.3. DLP of mullite substrates

Samples were additively manufactured using a DLP-based stereolithographic printer (Admaflex 130, Admatec Europe BV, Alkmaar, The Netherlands), which operates with a 405 nm wavelength UV light. The slurry was spread on a moving tape through a 125 μm doctor blade. To determine the curing depth, slurries were submitted to the UV light for different exposure times. The cured layers in a chessboard configuration were cleaned with paper to remove the uncured slurry and the thickness of the single layer was measured with a digital micrometre. After several tests, the curing parameters were optimized in order to provide the best compromise between high resolution, good adhesion, and uniformity of each layer. Therefore, a layer thickness of 30 μm, an exposure time of 1.2 s, and a LED power of 20.24 mW/cm^2 were fixed. A delay of 20 s before exposure was applied to let air bubbles be removed from the slurry.

Via this process, the following specimens, designed by AutoCAD software (Autodesk, San Francisco, CA, USA), were printed:

- Dense cylinders (diameter 1 cm, 0.5 cm height)
- Grid-like lattice cylinders (diameter 2.1 cm, 1.3 cm height)
- TPMS lattice cylinders (diameter 2.1 cm, 1.3 cm height)

2.14. Post-processing, sintering and characterization

After printing, the green bodies were submitted to a water debinding process for 4 h at 30 °C, to remove the uncured slurry as well as the hydro-soluble components of the resin, and then left overnight at room temperature. Then, the samples were oven-dried at 70 °C overnight before being submitted to thermal debinding and sintering processes, according to the treatment displayed in Fig. 1. Thermal treatments were performed in an electric furnace (Nabertherm, Nabertherm GmbH, Lilienthal, Germany) under air atmosphere. The slow heat treatment up to 400 °C is aimed at avoiding crack formation during resin decomposition. The geometrical density of the ceramic parts, ρ (g/cm^3) was determined by mass and geometric measurements. The density of the sintered samples was also determined by buoyancy method, following Archimedes' principle (Density Determination Kit, Sartorius YDK01, Göttingen, Germany). These sintered densities were then related to the theoretical density (TD) of mullite (3.17 g/cm^3).

The microstructures of sintered bodies were characterized by means of FESEM observations. The samples were previously gold sputtered (SPI Module Sputter Coater, West Chester, PA, USA).

2.2. Fabrication of MOFs-functionalized mullite substrates

2.2.1. Synthesis of HKUST-1

HKUST-1 seed crystals were synthetized by a solvothermal method, following the protocol proposed in [116] and schematically reported in Fig. 2. In a typical preparation, 2.16 g of $Cu(NO_3)_2{\cdot}3H_2O$ were dissolved in 30 mL of distilled water and 1.05 g of 1,3,5,-benzenetricarb-oxylic acid were dissolved in 30 mL of ethanol. Both reactants were supplied by Sigma-Aldrich (St. Louis, Missouri, USA) and used as received. The two solutions were mixed under stirring for about 30 min. The resulting precursor solution was then transferred into a hermetic Teflon bottle and heated at 120 °C for 6 h. The reaction vessel was then cooled naturally to room temperature. The resulting solution was labelled as solution A: it contained HKUST-1 crystals, unreacted ligands and copper species, and used as seeding solution on ceramic substrates.

2.2.2. Seeding and growth of HKUST-1 on mullite substrates

Prior to seeding, sintered mullite substrates were heated in an oven at 60 °C for 15 min. Ceramic samples were completely immersed in solution A and kept into the oven at 95 °C until complete solvents evaporation: the original protocol [37] was modified rising the temperature for this step at 95 °C to limit MOFs permanence in a water-rich environment. This seeding process was repeated three times to completely cover the ceramic surface with seed crystals. The seeded substrates were then washed with ethanol and sonicated for 1 min to remove crystals loosely attached to their surface. The three depositions, followed by ethanol washing and 1 min sonication, were repeated three

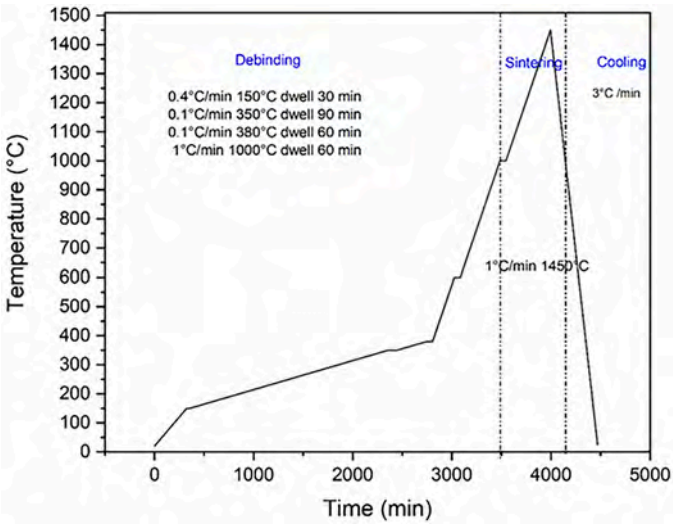

Fig. 1. Schematic diagram of thermal debinding and sintering cycles.

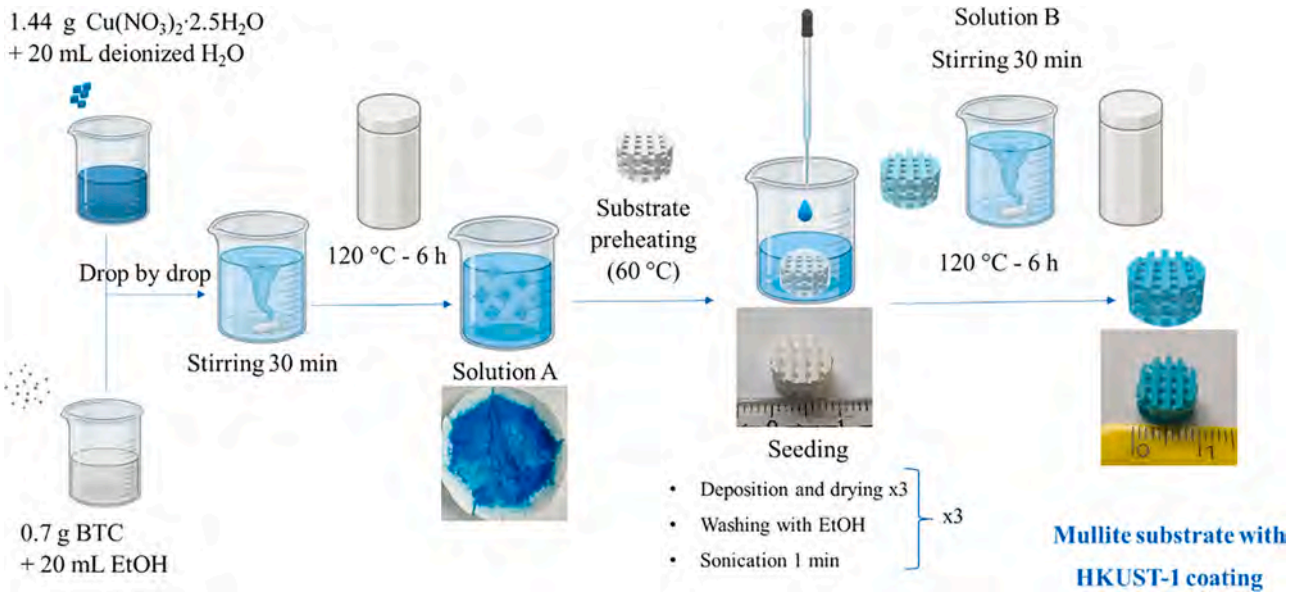

Fig. 2. Schematic illustration of the experimental procedure for HKUST-1 solvothermal synthesis, according to the protocol from [37].

times, so until the monoliths were uniformly coated with strongly bound seed crystals.

In a second step, the seeds deposited on the substrate were submitted to a growth stage. A second HKUST-1 solution was prepared by dissolving 1.09 g of $Cu(NO_3)_2{\cdot}3H_2O$ in 30 mL of water and 0.69 g of 1,3,5,-benzenetricarb-oxylic acid in 30 mL of ethanol. Then the two solutions were mixed and stirred for about 30 min, providing solution B. Meanwhile, seeded mullite substrates were placed in Teflon bottles, immersed in solution B, and transferred in an oven. After being heated at 120 °C for 6 h, the reaction vessel was then cooled naturally to room temperature. The samples were washed with ethanol and sonicated for 5 min to remove crystals loosely attached. Finally, the samples were dried under vacuum at 100 °C overnight. The overall scheme of the process is depicted in Fig. 2.

HKUST-1 crystals morphology and adhesion to the mullite substrates were characterized by means of FESEM observations. To evaluate specific surface area (SSA), pore volume and pore size of the synthetized MOFs, nitrogen physisorption tests were performed at – 196.15 °C (77 K) using the instrument TriStar II (Micromeritics, Norcross, GA, USA). Samples were degassed for 24 h under vacuum at 150 °C, in agreement with previous works [30,34].

2.2.3. Adsorption tests

CO_2 adsorption capacity of HKUST-1 powders as well as of coated and uncoated ceramic substrates were investigated in a flow-through reactor. The homemade experimental setup (Fig. S 1, a) consists of a tubular vertical furnace, an electronic control box for the bench (Siemens™, Berlin, Germany) and an analyser at the outlet of the reactor (μGC SRA 3000™). The time resolution of the analyser was of 2 min. A gas panel feeds a series of mass flow controllers. Helium was used as carrier gas, at two flow rates (3 L/h and 5 L/h) and the analyses were conducted at ambient pressure.

HKUST-1 seeds were tested as powdered material (around 100 mg) inserted into a quartz tube (Fig. S 1, b) while DLP-shaped mullite substrates were inserted into a microreactor with an aluminium foil to avoid gas leaks (Fig. S 1, c). In the powder bed experiments, the amount of HKUST-1 powder (ca. 100 mg) was chosen to correspond to the amount coated onto the monoliths. The powder was mixed with inert SiC to reach a height comparable to the monoliths (ca. 1.5 cm). For the DLP-shaped substrates, grid-like and TPMS architectures, both in the blank and HKUST-1 coated form, were studied. Further information about samples preparation is given in detail in SI.

Measurements were carried out as follows (Fig. S 2): i) stabilization of gas flow and CO_2 concentration at 30 °C and ambient pressure (1 atm) were needed to ensure the tests reliability; ii) adsorption measurements were performed at the same temperature and pressure, flowing 1% CO_2 in He flow (at 3 or 5 L/h) inside the reactor, before iii) a regeneration step, consisting in the heating of the sample from ambient temperature to 70 °C (at 5 °C/min), then to 120 °C (at 2 °C/min) for 4 h before a natural cooling to room temperature. CO_2 uptake was estimated by integration of the peak occurring in the outlet signal when the 1% CO_2 flow passed through the reactor. The total uptake amount during the adsorption time is obtained from the integral of the adsorption with time curves, from the beginning until the end of CO_2 uptake. Further details on CO_2 uptake are provided in the supplementary information.

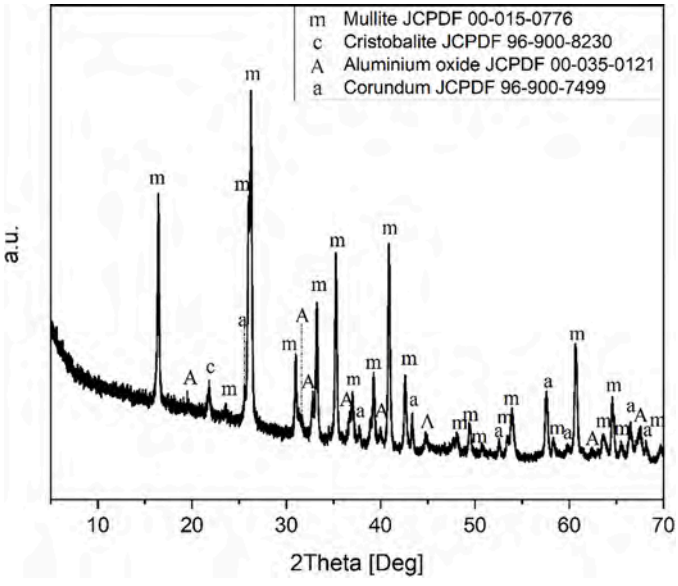

Fig. 3. XRD pattern of as received mullite powder.

3. Results and discussion

3.1. Powders characterization

3.1.1. Mullite powder

XRD pattern of the as-received mullite powder is depicted in Fig. 3. Mullite peaks were indexed according to the JCPDS file number 15–0776. A small fraction of aluminium oxide (Al_2O_3) was detected both in the hexagonal and monoclinic phase (respectively identified by JCPFD files 96–900–7499 and 035–0121). Finally, the peaks occurring at $2\theta \approx 21.8°$ is due to cristobalite (SiO_2), identified by JCPD file 96–900–8230.

The particle size distribution of mullite powder from laser granulometry is depicted in Fig. 4(a), whereas D_{10}, D_{50} and D_{90} values (corresponding to 10%, 50% and 90% of the cumulative volume distribution) are collected in Table 1. The as-received powder shows a multimodal distribution (black lines), with a D_{50} value corresponding to ~ 29 μm. A time of 5 min in a sonication bath was effective to significantly decrease the starting particle size: sonicated powder, in fact, reached a D_{50} of ~ 1.8 μm (red lines). Sonication reduced the size of the coarser fractions, as well depicted by the cumulative distributions represented by dot lines in Fig. 4(a): thus, it can be concluded the as-received powder is affected by soft agglomeration. The absence of hard clusters in the powder is desirable to ensure a good flowability and homogenization of the ceramic slurry. In Fig. 4(b), a FESEM micrograph of the as-received powder is depicted, showing micrometric agglomerates, made by nanometric primary particles.

Following already established protocols [100], 1% MgO sintering aid was mixed with the ceramic powders to optimise the sintering conditions and decrease the temperature of densification. This allows us tailoring the sintering temperature and substrate porosity. To do so, we studied the sintering behaviour of a green pressed bar by dilatometric analysis. The dilatometric curve up to 1,550 °C is depicted in Fig. 5(a) (solid line), showing that the material underwent a linear shrinkage of ≅ 15% during the heating stage. The derivative curve (dotted line) showed that the sintering onset temperature occurred at around 1,200 °C while the temperature corresponding to the maximum densification rate was determined to be 1,470 °C. The densification curve is depicted in Fig. 5(b), showing that the sample reached a geometrical density (ρ_{geom}) equivalent to 85.9% of theoretical density (TD of 3.17 g/cm^3 according to JCPDS file number 15–0776) (see Table 2). In order to increase the porosity in the sintered samples, which could be beneficial for the adhesion and growth of the HKUST-1 crystals, a second sintering cycle in which the sintering temperature was decreased to 1,450 °C was explored. In this case, a geometrical density of ≅ 65% with a highly porous microstructure (Fig. 5b, inset) was reached. FESEM observations of the sintered material showed a high coalescence of the acicular mullite grains during sintering at 1,550 °C. Even though porosity is partially still present, the higher density, in comparison to the part sintered at 1,450 °C, is clear. At lower sintering temperature, the microstructure remains highly microporous since the solid-state-diffusion, occurring at 1,450 °C, is not in a sufficient advanced phase to promote grain coalescence. Despite the high porosity, the sample holds sufficient mechanical strength to be handled. It should be also observed that the Archimedes' densities (ρ_{Arch}) were significantly higher, at precisely 90% and 94.6% TD for samples sintered at 1,450 °C and 1,550 °C, respectively. The huge difference between geometrical and Archimedes' density for the 1,450 °C-sample suggests that a high fraction of open pores is present in the material, as also indicated by the FESEM micrograph. According to these considerations, 1,450 °C was chosen as the optimal sintering temperature and used for the mullite-printed substrates.

Table 1
Particle size (μm) corresponding to 10% (D_{10}), 50% (D_{50}) and 90% (D_{90}) of the cumulative distribution (Fig. 4) of as-received and 5 min-sonicated mullite powders from laser granulometry.

	D_{10} (μm)	D_{50} (μm)	D_{90} (μm)
As received	0.90	28.70	106.00
5 min sonication	0.58	1.76	4.36

The influence of the sintering temperature on the porosity of mullite substrate after DLP was also studied by MIP. We used the dense pellet-like morphology for these studies. The opened porosity volume decreases together with the total pore area when increasing the sintering temperature (Table 3). The average pore diameter is more than five times lower for 1,450 °C sintered pellet, meaning that a 100 °C higher sintering temperature promotes pore coalescence. Both samples show a bimodal pore size distribution, but inverted peaks intensities (Fig. 6): the fraction of smaller porosity is more significant for the 1,450 °C sintered pellet. These results confirmed the previous FESEM observations and dilatometric measurements.

3.1.2. HKUST-1 powders

The crystals morphology of HKUST-1 seeds was observed via FESEM (Fig. 7(a)). The seed crystals exhibit a typical octahedral pyramid

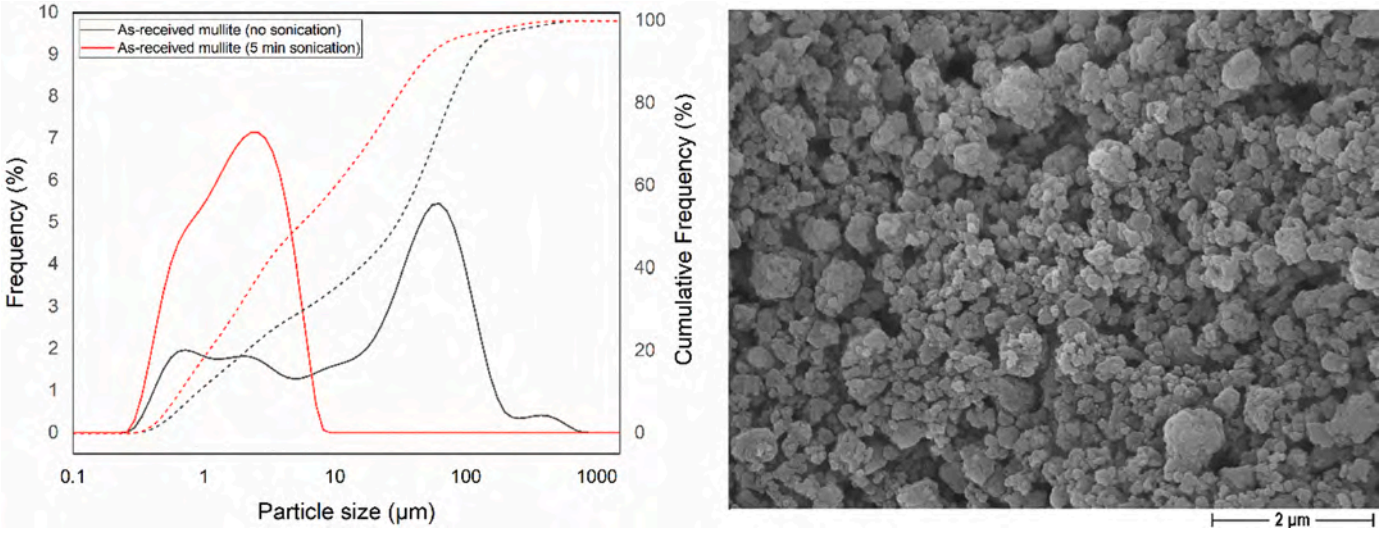

Fig. 4. (a) Particle size distribution of the as-received (dark lines) and 5 min-sonicated (red lines) mullite powder from laser granulometry. Frequency (solid lines) and cumulative frequency (dotted lines) curves are depicted. (b) FESEM micrograph of the as-received powder.

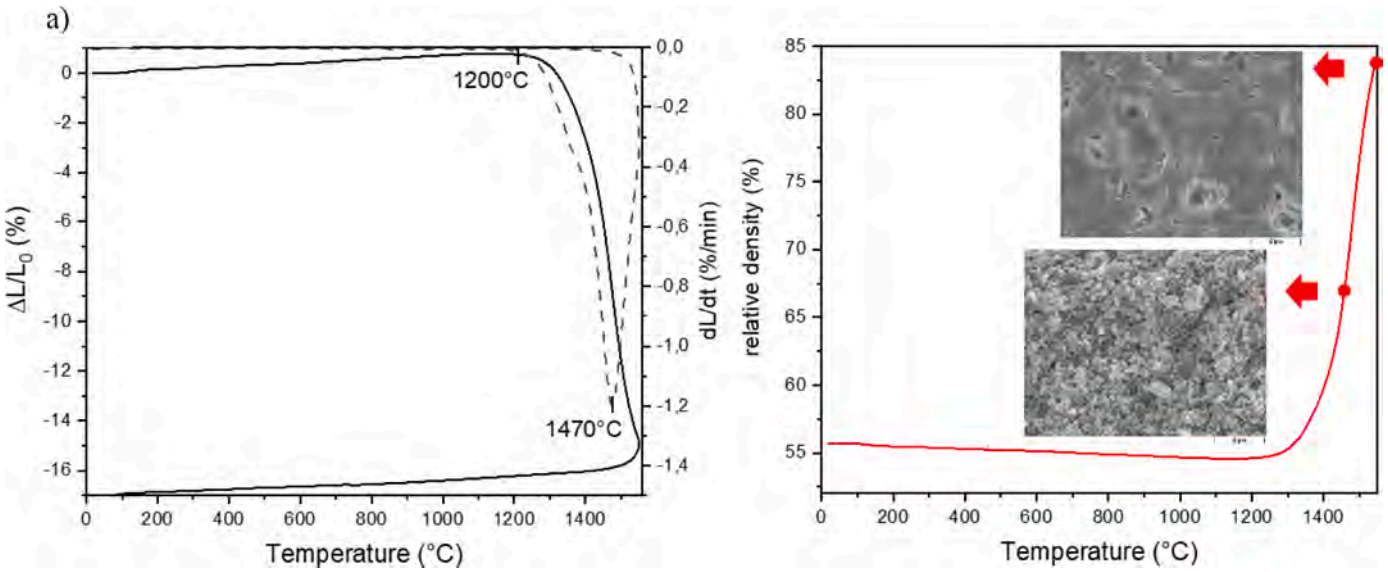

Fig. 5. (a) Dilatometric (solid line) and derivative (dotted lines) curve of mullite compact; (b) densification curve, showing the relative density and the microstructure of samples sintered at 1,450 °C and 1,550 °C.

Table 2
Characteristics of mullite pressed pellet sintered at 1,450 °C and 1,550 °C in terms of volumetric shrinkage, geometrical and Archimedes' density and HKUST-1 deposition amount.

Sintering T [°C]	1,450 °C	1,550 °C
Volumetric shrinkage [%]	14.5	37.5
ρ_{geom} [%]	62.6	85.9
ρ_{Arch} [%]	90.0	94.6
HKUST-1 deposition [wt%]	1.6	0.1

Table 3
Total intrusion volume, total pore area and average pore diameter of mullite sintered pellets as determined by MIP.

Sintering temperature	1,450 °C	1,550 °C
Total intrusion volume (at 29,986.59 psia) (mL/g)	0.2001	0.1394
Total pore area (at 29,986.59 psia) (m^2/g)	8.6	1.1
Average pore diameter (nm)	93.6	500.8

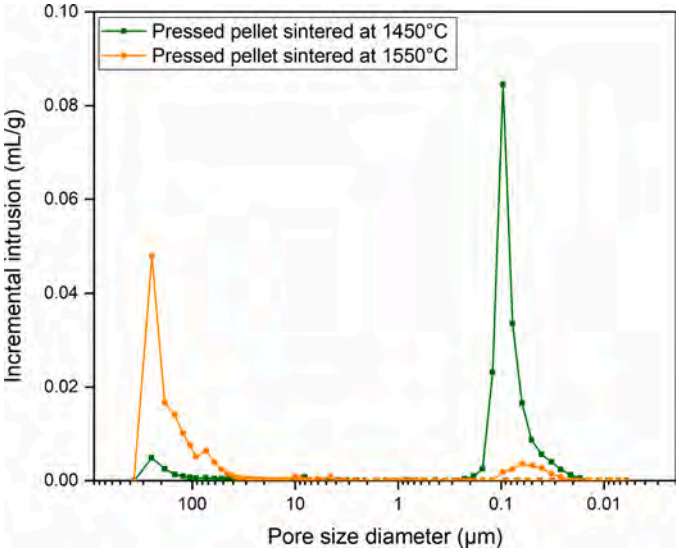

Fig. 6. Pore size distribution of pressed mullite pellets sintered at 1,450 °C (green line) and 1,550 °C (orange line).

structure and dimensions of the order of a few μm, these features being comparable with data reported in the literature [47,68,69,101]: this confirms the successful nucleation by solvothermal synthesis. However, a change in morphology occurred after the growth stage (Fig. 7(b)): the HKUST-1 seeds assemble in polyhedral or cuboctahedral morphologies, as already reported in literature [102]. The presence of such crystalline structures proved that the synthesis strategy made up of seed deposition and then crystal growth, was successfully performed.

To evaluate the crystalline purity of HKUST-1 crystals, XRD analyses were performed (Fig. 8, blue curve). Incomplete HKUST-1 crystallization, or incorrect stoichiometry, could lead to the presence of unreacted copper oxide species (Cu_2O or CuO) [47,103], which can significantly affect the adsorption properties of solids. XRD patterns of HKUST-1 crystals from the seeding solution (blue line) confirmed the successful formation of the MOF phase: in fact, the XRD patterns exhibited the same peaks as calculated patterns for HKUST-1 or previous experimental results from the literature [47,102–105]. The synthesized powder does not exhibit any peaks corresponding to CuO ($2\theta = 35.5°$ and 38.7°) or Cu_2O ($2\theta = 36.43°$) and hence can be related solely to $[Cu_3(BTC)_2]$. Moreover, the absence of significant impurities peaks at $2\theta = 11.0°$ [47, 103] confirms the high purity of HKUST-1 obtained from the solvothermal protocol employed in this study. As previously mentioned, water, present in our solvothermal protocol, could have had a high negative impact on the formation of well-defined HKUST-1 [106]. Our results hence show that a mixture of water and ethanol, followed by drying at temperatures close to 100 °C, to allow a fast evaporation of water, are a promising approach to mitigate the effect of water in the synthesis.

The CO_2 capturing properties of the synthesized MOFs and their capacity of interaction with CO_2 molecules correlate to the specific surface area (SSA) and porosity of HKUST-1 crystals. Nitrogen physisorption isotherms at 77 K were performed on both the nucleation seeds and the grown crystals, as depicted in Fig. 9. Both isotherms show a type IV shape, according to IUPAC classification [107]. In detail, the increase at low relative pressure (p/p_0 in the range 0–0.4) is related to the microporosity of HKUST-1, consistent with the two pores structures of diameter 0.9 and 0.35 nm. Surprisingly, a hysteresis loop is observed in both curves at $p/p_0 > 0.4$. This hysteresis is associated to a mesoporous

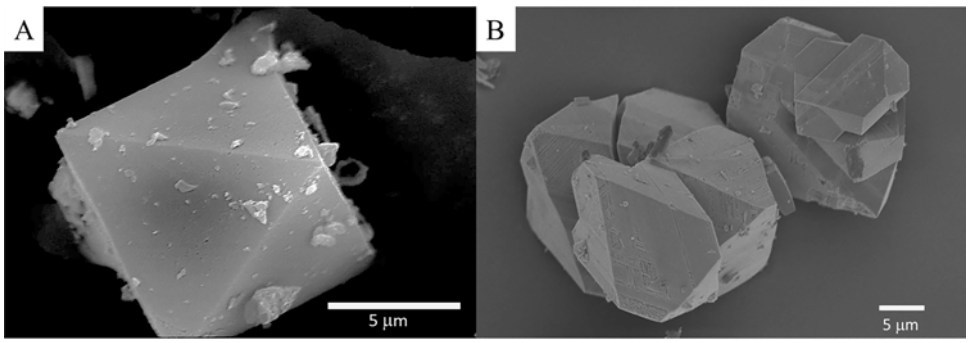

Fig. 7. FESEM micrographs of HKUST-1: tetrahedral seeds after nucleation (a) and cuboctahedral crystals after growth (b).

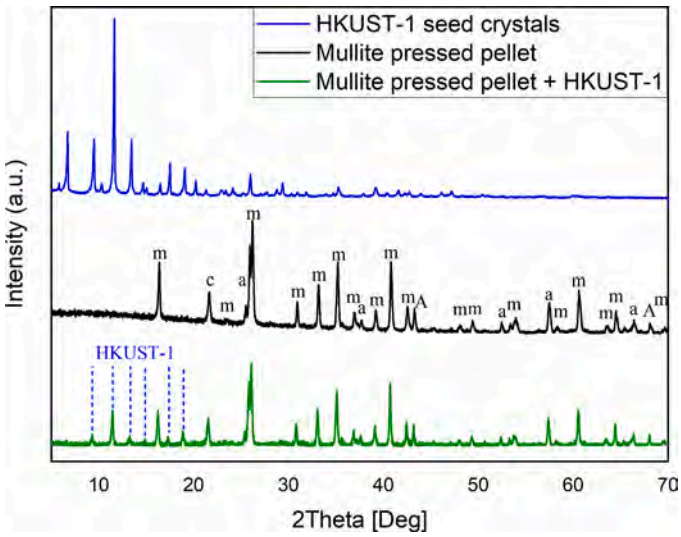

Fig. 8. XRD patterns of synthesized HKUST-1 (blue curve), mullite substrate in blank form (black curve) and after functionalization (green curve). In black, the peaks are related to mullite (m, JCPDF 00–015–0776), with small fractions of cristobalite (c, JCPDF 96–900–8230), corundum (a, JCPDF 96–900–7499) and alumina (A, JCPDF 00–035–0121), similarly to the mullite powder. In green, the peaks related to HKUST-1 are highlighted, the others are from the mullite substrate.

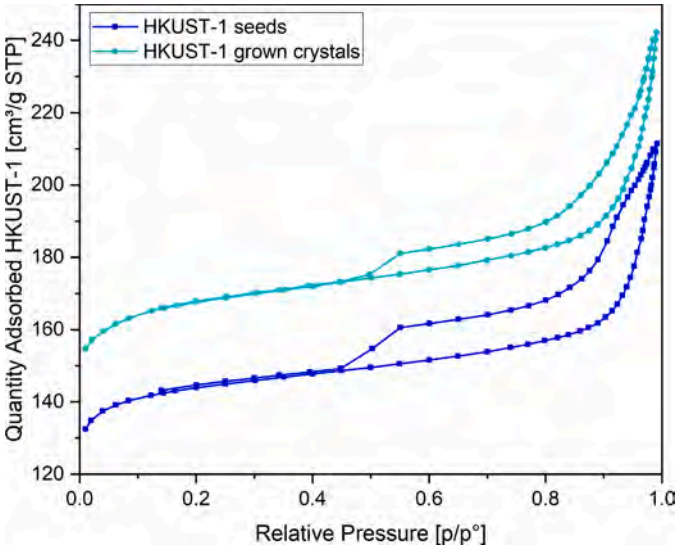

Fig. 9. N_2-sorption isotherms at 77 K for HKUST-1 seeds and grown crystals. Regeneration conditions: 24 h at 150 °C under vacuum.

structure. Indeed, the Barrett-Joyner-Halenda Model (BJH) approximation on the desorption branch allows extracting a mesoporous diameter of ca. 8 nm for both the seeds or grown HKUST-1 crystals. We interpretate this as the signature of particle aggregation and interparticle porosity, rather than from a mesoporous texture intrinsic of the material. Indeed, this has been observed previously for some HKUST-1 powders [69,108]. Nucleation seeds and grown crystals show similar isotherms trend: in fact, they are equivalent in terms of material nature. The main differences among the samples are related to the crystal's morphology, which influences textural properties. Grown crystals showed slightly higher SSA, resulting in a more efficient porous structure than seeds: thus, the growth step is fundamental not only to guarantee coating adhesion but also to enhance its porosity. This result seems promising for the CCS capacity of the systems, since the HKUST-1 functionalization on the ceramic substrates is made of grown crystals. Table 4 resumes the results in terms of SSA and pore volume obtained using the BET calculation. It is important to note that the specific surface area is lower than what is observed in the literature, while the pore volume, albeit consistent with some other results in the literature, could still be improved. Water, both present in our solvothermal treatment and after during storage of HKUST-1 as water vapours in ambient air may explain these underwhelming textural properties [32,106]: regarding the first possibility, our solvothermal synthesis could be optimized, notably by reducing the amount of water in the mixture and the drying step, while storage in vacuum may help for the second one. Nonetheless, this was not attempted as our goal is to design a procedure that can be easily industrially-scalable (hence avoiding harmful or complex solvents such as DMSO or complex storage), but also as HKUST-1 will anyway be in contact with water vapour in real life applications, we believe our protocol is a good approximation to estimate the CO_2 adsorption capacity of CCS MOF-mullite monoliths.

To check HKUST-1 adhesion and growth on mullite substrate and to investigate the role of mullite density, a first synthesis was performed on mullite pressed pellets sintered at either 1,450 °C or 1,550 °C. As shown by dilatometric graph in Fig. 6 and previously discussed, at 1,450 °C a higher porosity (≈35%) is obtained than at 1,550 °C (≈16%). This difference significantly affects the MOFs growth, as shown in Fig. 10. The presence of the turquoise-coloured layer on the white pellets confirms the adhesion of HKUST-1 to the porous mullite substrate. The sample with a higher porosity (left) is characterized by a more intense and

Table 4
Results of nitrogen adsorption analysis (77 K) in terms of SSA and pore volume (obtained via the BET method) and mesopores diameter (via the BJH desorption approximation) from the current study. Results are compared to diverse values from the literature.

	SSA [m^2/g]	Pore volume [cm^3/g]
HKUST-1 Seeds	433.40	0.32
HKUST-1 Grown Crystals	504.66	0.37
[8,28–36]	1,968–688.50	0.71–0.29

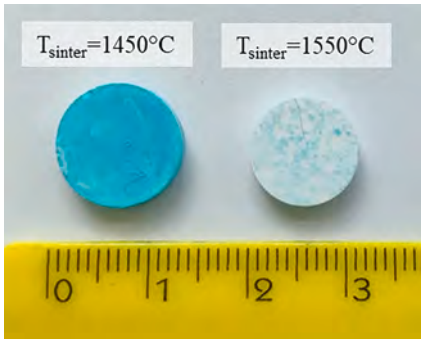

Fig. 10. Mullite pressed pellets sintered at 1,450 °C (left) and 1,550 °C (right), functionalized with HKUST-1.

homogeneous turquoise colour than the pellet sintered at 1,550 °C (right): consequently, as expected, HKUST-1 deposition (in terms of weight percentage) is significantly higher for the less dense pellet (see Table 2). Therefore, as expected, substrate inner porosity plays a crucial role in HKUST-1 adhesion: this confirms that 1,450 °C is preferable as sintering temperature than 1,550 °C.

Functionalized and blank pressed pellets, sintered at 1,450 °C, were analysed by XRD measurements to verify the presence and the chemical composition of the HKUST-1 coating. The patterns are compared to HKUST peaks in Fig. 8. Concerning the blank mullite support (black line), on top of peaks associated to mullite, the same previously discussed second-phases (α-Al_2O_3 and cristobalite) are occurring, even if with lower relative intensity compared to the as-received powder (Fig. 3), suggesting a certain reactivity during sintering. Finally, the XRD pattern of the mullite substrate coated with HKUST-1 crystals is depicted as well (green line): although the reflections of the mullite support have much higher intensities, when focussing on 2 theta angles in the range of the 5–20°, peaks corresponding to the MOF material are clearly evident [117]. Thus, $Cu_3(BTC)_2$ was successfully synthetized by seeding the support with micrometric crystals which, growing during the hydrothermal synthesis, effectively covered the substrate with a functionalization coating.

3.2. Elaboration and characterization of mullite slurries, 3D printing and functionalization of dense parts

The slurry used for additive manufacturing was prepared at 69 wt% solid loading (corresponding to 42.6 vol%), which was reached by the addition of 5 wt% dispersant (with respect to the mullite powder). Literature shows that a solid loading higher than 40 vol% is desirable to ensure a good densification of DLP processed materials [109]. High solid loading needs to be, however, combined with a correct rheological behaviour. Fig. 11 shows the evolution of the viscosity as a function of the shear rate. The desirable shear-thinning behaviour, characterized by a marked viscosity decrease as the shear rate increases, ensures a homogeneous spreading of the slurry on the tape during the DLP shaping [109,110].

Besides the necessary shear-thinning behaviour, it is important to check the shear viscosity at the operative shear rate, which corresponds to the shear rate applied by the blade on the slurry during its spreading. This value was identified at 160 s^{-1} in our process, corresponding to shear viscosity of ca. 1.4 Pa·s. Best formulations proposed in literature, usually show a viscosity lower than 3 Pa•s, to guarantee a good flowability [109]. Thus, the slurry formulation here proposed has a solid loading and a viscosity suitable for DLP.

This formulation was used to produce samples with different architectures by DLP. The first step was to realize simple dense designs, like pellets. The printed samples, after water and thermal debinding, were sintered at 1,450 °C, according to the preliminary tests described in §3.1.1. Table 5 summarizes the results in terms of shrinkage, geometrical

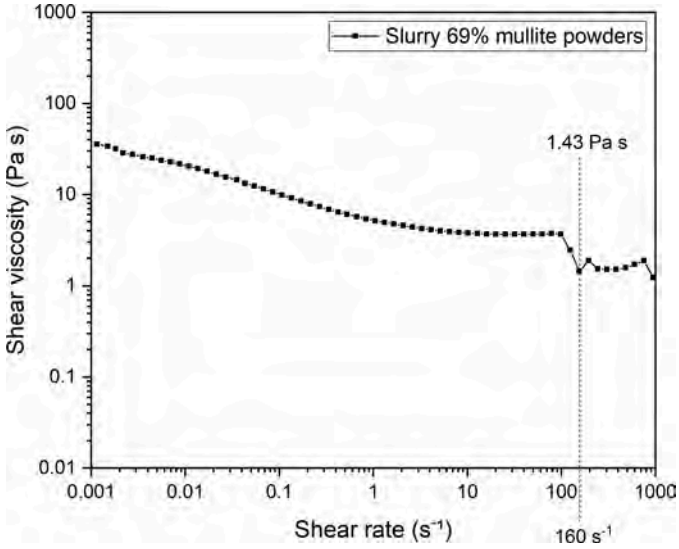

Fig. 11. Rheological curve of mullite slurry, prepared at 69 wt% solid loading and 5 wt% dispersant.The shear viscosity at the printing operative shear stress (160 s^{-1}) is highlighted.

Table 5
Properties of DLP shaped mullite samples, sintered at 1450 °C.

Printed sample property	Value
ρ_{geom} [%]	59.7 ± 0.5
ρ_{Arch} [%]	92.6 ± 3.1
x-y plane shrinkage [%]	9.4 ± 0.2
z direction shrinkage [%]	7.9 ± 0.7
Volumetric shrinkage [%]	24.5 ± 0.6

and Archimedes' density for dense samples. Since 3D printing is an anisotropic process, different shrinkage in different directions have been observed. The geometrical density obtained from printed sintered samples (≈ 60%TD) on one hand is high enough to guarantee a good mechanical stability and manageability of mullite structures; on the other hand, results are intentionally distant to the full densification to guarantee a desirable microporosity which could promote HKUST-1 crystals adhesion. The values obtained here are comparable but slightly lower in respect to pressed samples sintered at the same sintering temperature (ρ_{geom}≈65%). This was expected as, compared to a pressed green pellet, the mandatory addition of photopolymerizable polymeric medium, burned out before sintering, acts as an extra porogen agent [94,95]. The shrinkage among the printing direction (z) is surprisingly lower than in the x-y plane, meaning that the layer adhesion is good enough to limit the z-direction contraction. Fig. 12 shows representative FESEM micrographs of a printed and sintered bar. The lower magnification image (a) shows the layered structure of the 3D built material, having a layer dimension compatible with the nominal layer thickness set for printing (30 μm) and a good layer adhesion as no remarkable flaws can be observed at the interface between layers. In addition, the different micrographs at increasing magnifications (Fig. 12 (b) and (c)) show the presence of denser areas besides more porous ones, the former providing the sufficient mechanical strength for handleability of the ceramic substrate, the latter the required microporosity for MOFs adhesion and growth.

The 3D printed and sintered substrates were then functionalized by MOFs seeds, as described in §2.2.2. The successful functionalization of the mullite substrate by HKUST-1 was verified by FESEM observations, depicted in Fig. 13. HKUST-1 is grown from deposited nucleation seeds, forming onto the mullite support a continuous and homogeneous functionalized layer. Micrographs confirm both the formation of a

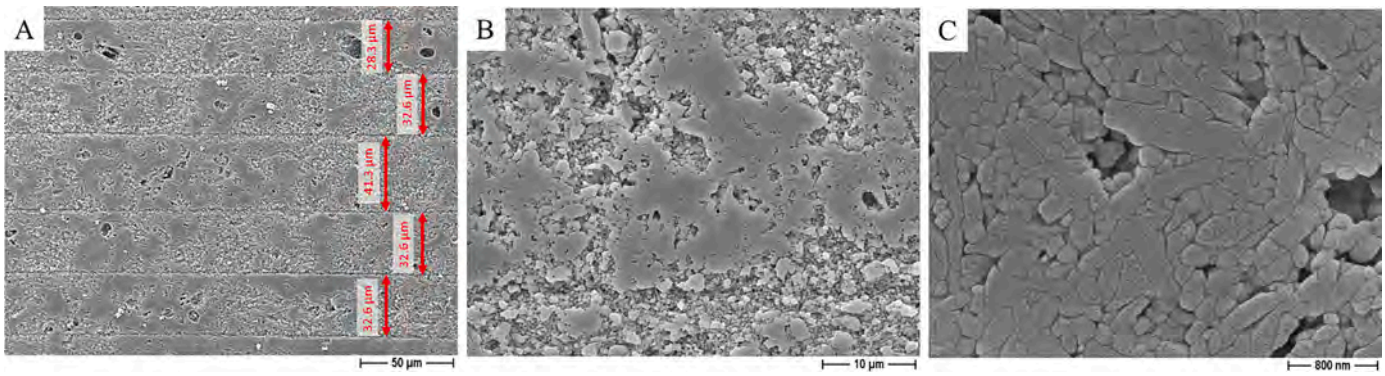

Fig. 12. FESEM micrographs of DLP-fabricated mullite structure.

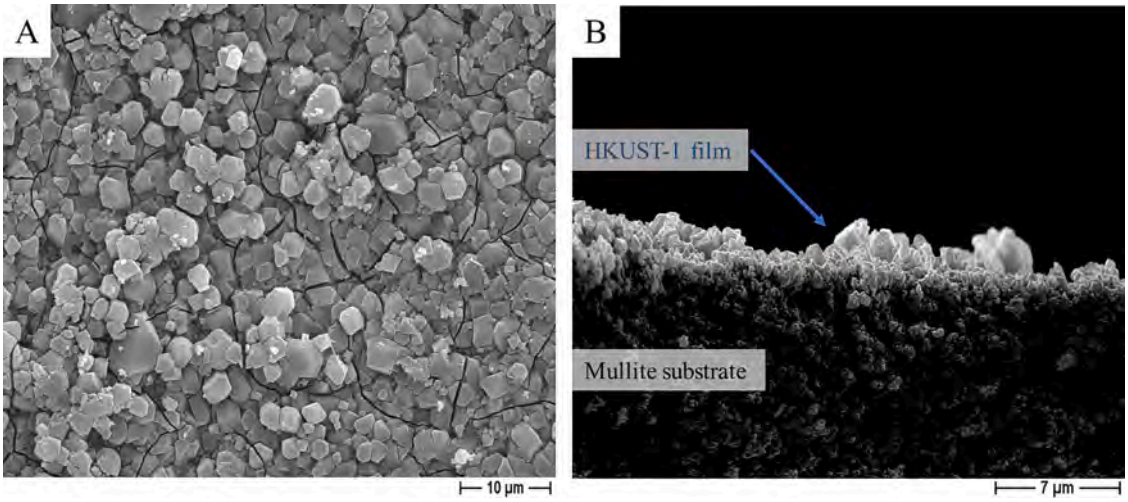

Fig. 13. FESEM micrographs of the HKUST-1 coating on DLP printed and sintered mullite substrate: top view of MOFs polyhedral grown crystals forming a homogeneous layer (a), cross-sectional view of the good quality mullite/grown HKUST-1 crystals interface (b).

homogenous and continuous coating, as well as the adhesion of HKUST-1 crystals on the substrate. Indeed, $Cu_3(BTC)_2$ crystals exhibit a polyhedral morphology and larger dimension than HKUST-1 seeds on the 3D printed substrate. After a second solvothermal synthesis at 120 °C in a Teflon hermetic bottle for HKUST-1 particles growth, crystals have increased in size and cracks developed running through neighbouring intergrown crystals Fig. 13 (a)): this is probably caused by differences in the coefficient of thermal expansion (CTE) between support and coating [68]. As typical for MOFs, HKUST-1 has a negative thermal expansion (CTE=-4.1×10^{-6}°C^{-1} [111]. This is due to the thermal excitation of vibrational modes within the organic linkers: the shrinkage of their longitudinal extension causes a contraction of the structure. Thus, upon heating, stress occurs in MOF thin films firmly adherent to a ceramic support with positive thermal expansion coefficient, such as mullite (4–5 $\times 10^{-6}$°C^{-1} [112]), which on the contrary expand upon heating. This stress may induce internal microcracking or lead to delamination of MOFs coating from the substrate [113]. Therefore, the shown result on one hand confirms the good adhesion with the porous support. On the other hand, it suggests that crystals dimension must be controlled [68], to limit interfacial stress during the film formation and guarantee the MOFs grafting on the ceramic pores. Cross-sectional view in Fig. 13(b) highlights intergrowth between crystals and a good quality interface between mullite and MOFs grown crystals. The continuous and homogeneous MOFs layer here obtained can be considered an ideal candidate due its cross-linked structure and the presence of free carboxylic groups, which facilitate the attachment of this compound to the porous ceramic surface [68]. In addition, a homogeneous turquoise coloration due to the HKUST-1 coating can be macroscopically observed in Fig. 14, (e) and (f).

3.3. 3D printing and functionalization of complex architectures

After optimizing the printing process for dense specimens of simple geometry, our attention was focused on the shaping of lattice ceramic architectures: two designs were obtained by CAD software and are shown in Fig. 14 (a and b), whereas Table 6 summarizes their nominal characteristics. The grid-like architecture was selected since it is widely used for gas filtering applications [114,115],. The main drawback related to grid-like lattices are related to sharp edges (Fig. 14(a)): they may cause limitations in the coating adhesion and gas/surface contact. Thus, Triply Periodic Minimal Surfaces have been also tested, in particular with a Schwartz Primitive structure: TPMS are promising designs for several applications due to their smooth surfaces (Fig. 14(b)) and high porosity [72,79] . Comparing the two selected architectures, for almost the same surface area, TPMS requires less volume and provides a tripled surface to volume ratio (Table 6): thus, it seems more promising for CCS applications. To verify this hypothesis, both architectures were printed through DLP and sintered at 1,450 °C, (Fig. 14(c) and (d)), then coated with HKUST-1 (Fig. 14(e) and (f)).

Once identified the optimal conditions to grow MOF crystals on simple mullite DLP-fabricated pellets, the next step was to develop a MOFs coating on the complex grid-like lattice and TPMS structures. To produce a complete coverage and achieve a homogeneous coating, the two complex structures were submitted to several seeding/growth processes (as described in §2.2.2), and the efficiency of the deposition

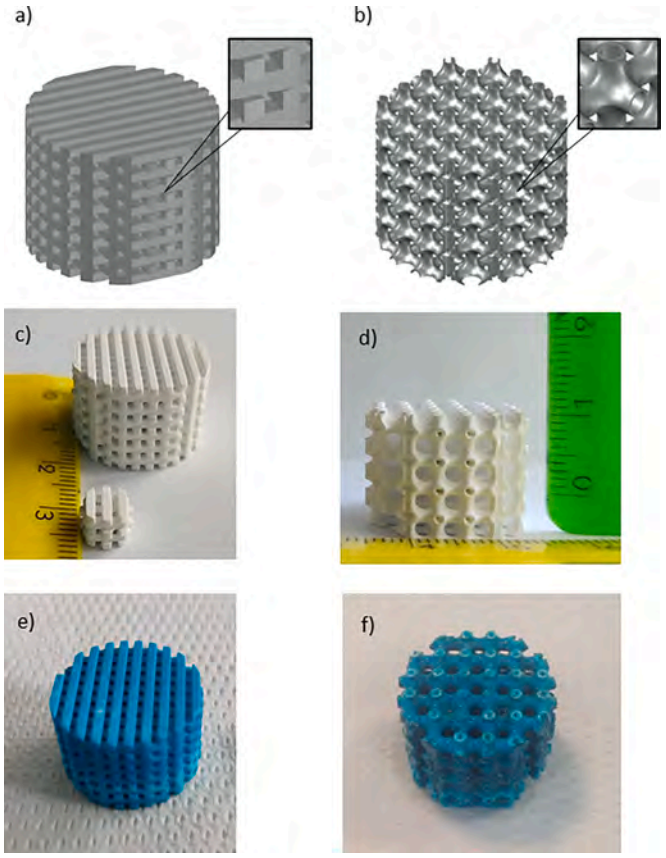

Fig. 14. (a, b) CAD files, (c, d) 3D printed blank and (e, f) functionalized monoliths with grid-like (a,c,e) and Schwartz primitive TPMS (b,d,f) architecture.

Table 6
Nominal properties of the CAD files for grid-like and Schwartz Primitive TPMS monoliths.

Nominal property	Grid-like structure	TPMS
Surface area [mm^2]	7,268.12	7,245.55
Volume [mm^3]	2,363.66	775.47
SA:V ratio [mm^{-1}]	3.08	9.34
Weight [g]	7.49	2.46
SSA [mm^2/g]	970	2,947

process was monitored in terms of weight variation. An example is provided in Fig. S 4 (SI) for the TPMS structure. Each deposition results in an increase of the HKUST-1 wt percentage, but a decrease is observed after each EtOH washing, performed to clean the sample from any crystals in excess, not completely adhering to the surface. At the end of the process, an average final weight mass increase of about 1.7% and 3.5% were determined for the grid-like and TPMS structures, respectively. Thus, TPMS designs demonstrated a doubled uptake of HKUST-1 in wt% in respect to grid-like lattice monoliths. Compared to the sharp edges of the grid-like design, the smooth and interconnected TPMS surface seems to promote a better MOFs adhesion. The higher HKUST-1 percentage of the TPMS compared to the grid-like structure enhances the functionalization degree and CO_2 adsorption capacity of the material, a key property for CCS system.

3.4. CO_2 adsorption tests

Preliminary tests in the bench were performed using first the HKUST-1 seeded crystals at various CO_2 concentration (Fig. S 5, SI). As expected, the CO_2 uptake increases with the CO_2 concentration in the gas flow. The highest CO_2 concentration achievable with our setup, 1%, was then used for the adsorption studies. A crucial role in the investigation of CO_2 adsorption capacity is the regeneration process. Several studies have demonstrated that CO_2 adsorption on HKUST-1 is completely reversible, and that the full adsorbent regeneration can be obtained raising the temperature under inert flow or under vacuum [28,32]. In the current study, HKUST-1 regeneration is performed under a helium flow of 3 L/h, keeping the samples at 120 °C for 4 h. During regeneration, a drastic change of colour, from light cyan to Prussian blue, is observed for MOFs powders (see Fig. S 6, SI). This colour shift is the macroscopic effect of the change in symmetry of copper ions: water removal from Cu^{2+} coordination sphere, due to the temperature increase, produces a loss of degeneracy in d levels and the availability of new d-d transitions [25].

CO_2 uptake profiles for the HKUST-1 powder bed, the grid-like (GL) and TPMS monoliths, both without (blank) and with HKUST-1, are shown in Fig. 15. Steeper slopes and significantly larger areas under the curves for functionalized monoliths compared to either blanks or powder bed are observed. Let us note that, due to the 2 min time resolution of the μGC analyser, the breakthrough time cannot be measured accurately.

Total CO_2 uptakes are estimated at two specific flow rates and evaluated from the integration of CO_2 adsorbed versus time curves and are shown in Fig. 16. Firstly, the gas flow conditions, chosen in accordance with literature [36,43,67] are significantly impacting the adsorption mechanism with a decrease of the amount of adsorbed CO_2 when the gas flow increases, as previously observed in the literature [116]. Secondly, comparing the blank and functionalized systems (Fig. 16(a)), results clearly show that the amount of CO_2 adsorbed is increased for the coated monoliths compared to the blanks. Interestingly, blank samples seem to also interact weakly with CO_2: a possible interaction could occur between the positive dipole of the CO_2 molecules and the –OH groups on the ceramic surface, but the nature, stability and durability of this effect are not clear and would require a study of their own. Thirdly, when comparing the results obtained between HKUST-1 powder and coated monoliths, we have normalised the amount of CO_2 adsorbed by the mass of HKUST-1 used to evidence the influence of shaping (Fig. 16(b)). Results clearly show that, for the same amount of HKUST-1, the CO_2 intake for both coated monoliths is higher compared to the powder bed. In detail, compared to HKUST-1 powder bed, 3D printed mullite structures functionalized with $Cu_3(BTC)_2$ led to a CO_2 uptake increase up to 40.1% and 51.3% for grid-like and TPMS geometries (in terms of mg of CO_2 for each gram of HKUST-1). This increase in the uptake from the monoliths compared to the powder may be related to a better accessibility to the active sites thanks to the macroporosity. The Schwartz primitive is providing the best results, both in term of total CO_2 uptake (Fig. 16(a)) than when normalised to the amount of HKUST-1 (Fig. 16(b)). The higher surface-to-volume ratio (see Table 6) and high specific surface area of TPMS enhances the HKUST-1 loading (3.5% for TPMS versus 1.7% for the grid-like) explaining the former, while the more complex architecture and tortuosity would help increase the contact time between CO_2 molecules and active sites and hence the latter. Data hence are confirming the key role played by complex design supports with interconnected and highly porous architectures. The great potential of DLP as ceramic shaping process is asserted too as it allows designing easily such complex geometries.

Although this work is not focused on the system durability, to ensure reliable results and guarantee the reproducibility of the CO_2 storage properties of our powders and monoliths, all samples have been tested at least twice. The experimental error bars are significant especially at higher flow; thus, the 3 L/h gas flow allowed in general to obtain more reliable results. No loss of capacity over time was observed in these conditions. The system is equipped to measure pressure at inlet and outlet of reactor, ensuring a constant pressure of 1 atm during test. In the employed tests conditions (low samples height, gas flow and SiC coarse granulometry), no relevant differences between monoliths and powder were observed.

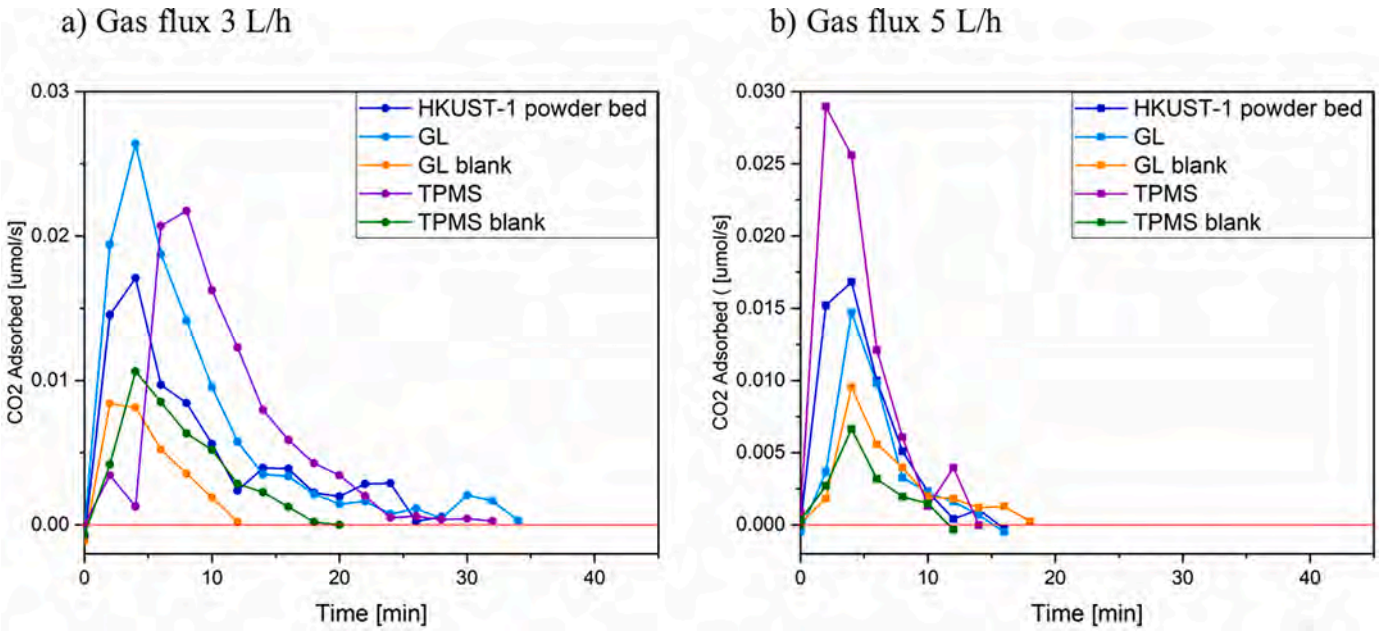

Fig. 15. CO_2 uptake with time for HKUST-1powder bed, blank and MOFs functionalized Grid-like (GL) and TPMS monoliths. Samples tested into the bench with 1% CO_2 after regeneration at 120 °C for 4 h with two different gas flows.

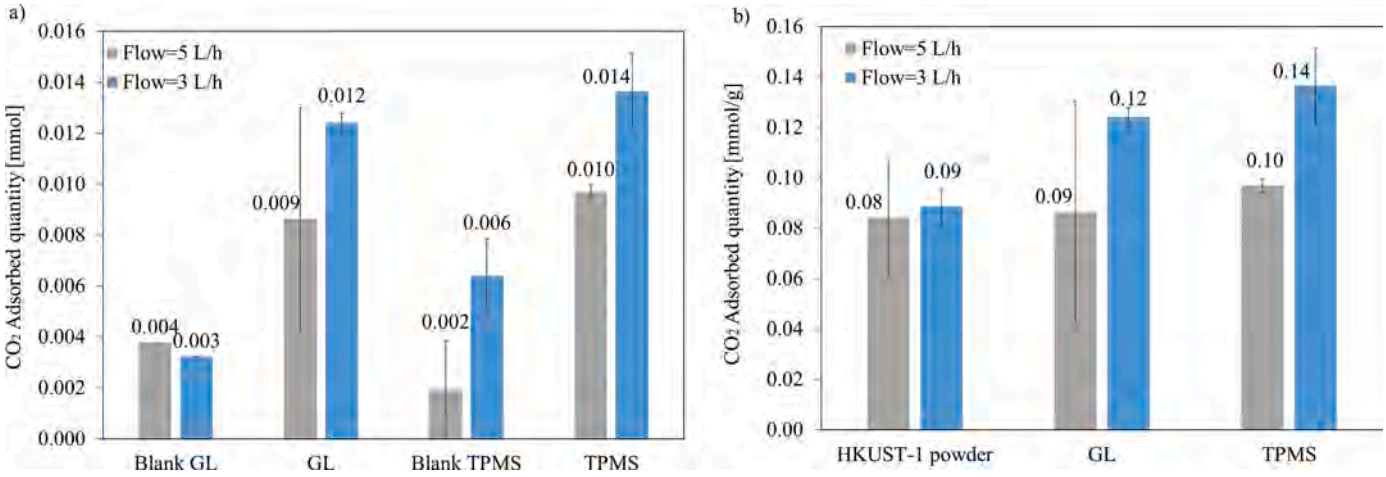

Fig. 16. Results from CO_2 adsorption measurements: a) mmol of CO_2 adsorbed by blank or HKUST-coated monoliths with the grid-like (GL) or TPMS network. For each network, both blank and HKUST-coated monoliths exhibited the same dimensions. B) mmol of CO_2 per g of HKUST-1 for MOFs powder and functionalized grid-like (GL) and TPMS monoliths. All samples were tested after regeneration (at 120 °C for 4 h under He flow) and with similar conditions (see Materials and methods). Experimental error bars are the standard deviation from two analyses, except for the blank GL.

Table 7 provides a comparison between our results with studies on HKUST-1 used for CO_2 capturing in various shaping (powders or composites).

Different testing conditions are responsible for most of the uptake variations. Regeneration parameters are crucial for MOFs response, and it has to be highlighted that here HKUST-1 was not activated in high vacuum. In addition, only a low CO_2 concentration (1%) is allowed by the installation. Thus, a future perspective is to increase CO_2 concentration for the inlet gas flow in order to evaluate the material response in more realistic conditions in respect to gas flow and CO_2 concentration, and study in more detail breakthrough curves. Among investigations on HKUST-1, the study by *Liu* et al. [36] led to a CO_2 uptake in mg per g of HKUST-1 of 24.21 mg/g (0.55 mmol/g), using a HKUST-1 and Ni/DOBDC system, the same flow rate of 3 L/h but a doubled CO_2 concentration ([CO_2]=2%) and a different activation process (2 regeneration steps, 170 °C, 8 h under vacuum and 170 °C). Thus, at the testing conditions applied, CO_2 uptake values reported here can be considered in line with previous studies.

It is also interesting to compare our materials to other types of textured CCS systems currently investigated in the literature. The current most promising CCS include amine functionalised silica [89], zeolites monoliths made via robocasting [46], MOF-polymer composites made by robocasting [43] or currently used activated carbons [121]. Table 8 gives the SSA and CO_2 uptake from those materials. Although the methods for measuring the CO_2-sorption capacity may differ and may not be directly comparable, notably as most examples were studied at much higher concentration of CO_2, it can be observed that most of these examples exhibit higher CO_2 uptake than our current study, with Zeolite 13X shaped with robocasting exhibiting a sorption capacity almost ten times higher than the current study. This highlights the importance of the total amount of active phase in the composite, as the samples made via robocasting can exhibit up to 90% of active phase and

Table 7
Comparison of CO_2 intake for HKUST-1 powder bed, DLP-shaped monoliths found in this study with various results from the literature. In each case, the adsorption and regeneration conditions are provided.

Study	CO_2 uptake Adsorption conditions					Regeneration conditions		
	[mmol/g]	CO_2 [%][1]	Flow [L/h][1]	T [°C]	P [bar]	T [°C]	t [h]	Atmosphere
HKUST-1	0.096	1	3.00	30	1.01325	120	4	He
GL	0.128	1	3.00	30	1.01325	120	4	He
TPMS	0.151	1	3.00	30	1.01325	120	4	He
[36]	0.55	2	3.00			170, 170	8, 12	vacuum
[23]	1.82			30	10			
[117]	3.27			25	1			
[23]	4.2	Pure (30 min)	6 N_2 and 1.98 CO_2	27	1	150, 27	30min	N_2
[38]	4.5			22	0.9			
[33]	7.23	pure		65	1.01325	180	8	vacuum
[118]	8.07	99.999		30	10	150	overnight	vacuum
[119]	0.8			25	1	160	3	vacuum
[32]	1.75			45–60	0–1	100, 200	3, 8	vacuum
[28]	2.88	99.999		25	1	150	2	vacuum
[30]	6.85	99.999		23	1	150	8	vacuum
[8]	≈10			amb	42			inert
[35]	≈18			35	100	150	12	0.3 Pa
[120]	6.13	99.999		0	1	150	8	vacuum

[1] For some studies flow and gas concentration are not specified: usually, in this cases, adsorption isotherms analysis was performed and pure CO_2 use is assumed.

Table 8
Some examples of textured CCS systems reported in the literature.

CCS Material	**Shaping**			**CO_2 uptake Adsorption conditions**					**Ref**
	Technique	Substrate	Sorbent wt%	CO_2 uptake [mmol/g]	CO_2 [%]	Flow [L/h]	T [°C]	P [bar]	
HKUST-1	DLP	Coated mullite (GL)	1.7	0.128	1	3	30	1.01325	This
	DLP	Coated Mullite (TPMS)	3.5	0.151	1	3	30	1.01325	study
MOF-74	Extrusion	Coated Cordierite	52	1.5	10	3.6	25	1.01325	[67]
UTSA-16	Extrusion	Coated Cordierite	55	0.6	10	3.6	25	1.01325	
MOF-74	Robocasting	bentonite clay and PVA	80	1.35	0.5	3.6	25	1	[43]
UTSA-16	Robocasting	bentonite clay and PVA	85	1.31	0.5	3.6	25	1	
MOF-74	Robocasting	Secondary growth on Torlon	≈40	2.5	10	3.6	25	1.01325	[42]
HKUST-1	Robocasting	Torlon	60	1.2	10	3.6	25	1.01325	
13X zeolite	Robocasting	Bentonite clay; Methyl cellulose and PVA removed by calcination	90	1.93	0.5	3.6	25	1.01325	[46]
5A zeolite	Robocasting	Bentonite clay; Methyl cellulose and PVA removed by calcination	90	1.94	0.5	3.6	25	1.01325	
Amine functionalized silica sorbents	DLP	Amine grafted silica	2.8 mmol/g	0.66	100	–	70	0.1	[89]
Active carbons	SLA			3.17	15	10	40	1.2	[121]

suggests further optimisation of our impregnation procedure should be implemented, both to improve the textural properties of the HKUST-1 synthesised and the amount of active phase added to the support. Interestingly, CCS made using MOF-74 and UTSA-16 via robocasting also present remarkable CO_2-sorption properties, despite the reduction in SSA from the presence of the binder. Our procedure could be extended to other types of MOFs to further tune our CO_2 uptake. Moreover, other important parameters than the CO_2 uptake should be considered such as the processability, the selectivity towards CO_2, regeneration, durability, effect of shaping among other to finely evaluate the properties of any CCS. For example, active carbon, extensively used due to its cheapness, is poorly selective. Further works on our materials will include notably the study of their selectivity towards water.

In conclusion, our work combines for the first time the formation of monoliths exhibiting highly complex architecture of high resolution using DLP with the surface functionalisation using MOFs to form new CCS composites. Despite the limited adsorbent mass incorporated on the supports surface (3.5 wt%), the MOFs/mullite system showed a promising interaction with CO_2 in the bench tests: the novelty proved in this preliminary study is the key role of substrate geometry and SSA in enhancing both HKUST-1 deposition and contact time between the adsorbent phase and CO_2 molecules. Thus, an accurate model of complex substrate geometry, eventually increasing the cell number, is a promising focus for future investigations in order to optimise CCS properties of such systems.

4. Conclusion

Complex porous mullite parts were successfully printed by DLP using slurries with a solid loading of 69 wt% in a photocurable resin, with the help of a dispersant at 5 wt% in respect to the ceramic powder. The slurry exhibited rheological properties suitable for printing, with a shear thinning behaviour and a shear viscosity of 1.4 Pa·s at the printing operative shear stress (160 s^{-1}). Then, the best printing parameters were found fixing the layer thickness at 30 μm, the exposure time at 1.2 s, the LED power at 20.24 mW/cm^2 and the delay before exposure at 20 s. High resolution of the DLP process allowed to precisely shape geometrically complex monoliths with grid-like and Schwartz primitive TPMS design.

Highly pure HKUST-1 crystals were successfully synthetized by a two-step solvothermal synthesis process based on crystal nucleation and subsequent growth. The method was adapted, using a 9 steps deposition, to functionalise 3D printed mullite monoliths with homogeneous $Cu_3(BTC)_2$ coatings. The amount of HKUST-1 coated was estimated by studying the mass intake for both the grid-like and TPMS geometries, and the results showed that more HKUST-1 were deposited on the TPMS

samples, with a mass intake of 3.5% compared to 1.7% for the grid-like structure.

CO_2 adsorption tests performed in a catalytic bench reactor under 1% CO_2 gas flow (99% He) provided encouraging results. Before adsorption measurements, samples were always regenerated under helium at 120 °C for 4 h. Up to three cycles of regeneration-adsorption studies were done without any loss of the adsorption capacity of the HKUST-1 powder or the coated materials. Coated ceramic lattices showed a higher uptake than HKUST-1 powder, demonstrating the importance of a support in enhancing the uptake efficiency. Compared to HKUST-1 powder bed, 3D printed mullite monoliths functionalized with $Cu_3(BTC)_2$ led to a CO_2 uptake increase of 40.1% and 51.3%, for grid-like and TPMS geometries respectively.

Thus, TPMS designs showed the best results both in term of HKUST-1 loading and CO_2 adsorption, confirming the key role played by complex design supports and the great potential of DLP as a ceramic shaping process. A geometrically complex and porous ceramic support provides several advantages: on one hand, it guarantees a good handling of the CCS system, avoiding issues related to the use of powders alone (e.g. powder bed stacking, pressure drops). On the other hand, it enhances the accessibility of the active sites thanks to the formation of shaped macropores, thus increasing the adsorption capacity in respect to the same amount of active sorbent in form of powder bed. However, further developments are needed to increase the efficiency of the engineered CCS systems and enhance adsorbed CO_2 amount. Furthermore, as HKUST-1 is sensitive to moisture, future works focusing on the selectivity of these HKUST-1 coated monoliths towards CO_2 and water will be carried. In any case, the current work paves the way for the design of CCS tailored both in term of architecture than chemical selectivity towards CO_2.

CRediT authorship contribution statement

Arianna Bertero: Writing – review & editing, Writing – original draft, Methodology, Investigation, Formal analysis. **Julien Schmitt:** Writing – review & editing, Supervision, Methodology, Formal analysis, Conceptualization. **Helena Kaper:** Writing – review & editing, Supervision, Methodology, Formal analysis, Conceptualization. **Bartolomeo Coppola:** Writing – review & editing, Supervision, Methodology, Investigation, Formal analysis, Conceptualization. **Paola Palmero:** Writing – review & editing, Supervision, Methodology, Formal analysis, Conceptualization. **Jean-Marc Tulliani:** Writing – review & editing, Supervision, Methodology, Formal analysis, Conceptualization.

Declaration of competing interest

The authors declare the following financial interests/personal relationships which may be considered as potential competing interests:

Arianna Bertero reports financial support and travel were provided by European project AMITIE. Paola Palmero reports a relationship with European project AMITIE that includes: funding grants. If there are other authors, they declare that they have no known competing financial interests or personal relationships that could have appeared to influence the work reported in this paper.

Data availability

Data will be made available on request.

Acknowledgments

The Authors greatly acknowledge the Interdepartmental laboratory SISCON (Safety of Infrastructures and Constructions) from Politecnico di Torino for the use of the rheometer and of the mercury porosimeter. The work has been developed in the framework of the European project AMITIE, Additive Manufacturing Initiative for Transnational Innovation in Europe, Research UE - H2020 - Excellent Science - Marie Skłodowska Curie Grant Agreement n°734342. This publication is part of the project NODES which has received funding from the MUR – M4C2 1.5 of PNRR funded by the European Union - NextGenerationEU (Grant agreement no. ECS00000036).

Supplementary materials

Supplementary material associated with this article can be found, in the online version, at doi:10.1016/j.apmt.2024.102407.

References

[1] Carbon Cycle Greenhouse Gases. https://gml.noaa.gov/ccgg/, 2024 (accessed 30 August 2024).
[2] How Do We Know the Build-Up of Carbon Dioxide in the Atmosphere is Caused By humans? , https://www.climate.gov/news-features/climate-qa/how-do-we-know-build-carbon-dioxide-atmosphere-caused-humans 2024 (accessed 30 August 2024).
[3] IPCC. Sections. In: Climate Change 2023: Synthesis Report. Contribution of Working Groups I, II and III to the Sixth Assessment Report of the Intergovernmental Panel on Climate Change, Core Writing Team, IPCC, Geneva, Switzerland, 2023, pp. 35–115, https://doi.org/10.59327/IPCC/AR6-9789291691647.
[4] Paris agreement. https://treaties.un.org/Pages/ViewDetails.aspx?src=TREATY&mtdsg_no=XXVII-7 2015 (accessed 30 August 2024).
[5] Energy Technology Perspectives 2020, Special Report on Carbon Capture Utilisation and Storage, CCUS in Clean Energy Transitions. https://efaidnbmnnnibpcajpcglclefindmkaj/, https://iea.blob.core.windows.net/assets/181b48b4-323f-454d-96fb-0bb1889d96a9/CCUS_in_clean_energy_transitions.pdf, 2020 (Accessed 30 August 2024).
[6] T. Ghanbari, F. Abnisa, W.M.A. Wan Daud, A review on production of metal organic frameworks (MOF) for CO_2 adsorption, Sci. Total Environ. 707 (10) (2020) 135090, https://doi.org/10.1016/j.scitotenv.2019.135090.
[7] M. Sai Bhargava Reddy, D. Ponnamma, K.K. Sadasivuni, B. Kumar, A. M. Abdullah, Carbon dioxide adsorption based on porous materials, RSC Adv. 11 (2021) 12658–12681, https://doi.org/10.1039/d0ra10902a.
[8] A.R. Millward, O.M. Yaghi, Metal-organic frameworks with exceptionally high capacity for storage of carbon dioxide at room temperature, J. Am. Chem. Soc. 127 (51) (2005) 17998–17999, https://doi.org/10.1021/ja0570032.
[9] L. Gao, Y. Deng, H. Liu, K. Solomon, B. Zhang, H. Cai, Detection of Pb2+ in Tea Using Aptamer Labeled with AIEgen Nanospheres Based on MOFs Sensors, Biosensors. 12 (9) (2022), https://doi.org/10.3390/bios12090745.
[10] H. Li, X. He, M. Zhang, X. Li, R. Wang, Z. Xu, F. Li, Postsynthesis strategy of functional Zn-MOF sensors for the detection of ClO-and DPA, Inorg. Chem. 60 (4) (2021) 2590–2597, https://doi.org/10.1021/acs.inorgchem.0c03468.
[11] B. Sun, T. Tao, L. Liu, R. Ding, Y. Mao, Electron transfer facilitated by π-π stacking during the nitrobenzene recognition process of an MOF sensor, J. Phys. Chem. C. 125 (22) (2021) 12433–12440, https://doi.org/10.1021/acs.jpcc.1c02942.
[12] G.J. Lee, Y.W. Chien, S. Anandan, C. Lv, J. Dong, J.J. Wu, Fabrication of metal-doped BiOI/MOF composite photocatalysts with enhanced photocatalytic performance, Int. J. Hydrogen. Energy. 46 (8) (2021) 5949–5962, https://doi.org/10.1016/j.ijhydene.2020.03.254.
[13] Y. Xue, X. Zhou, Y. Zhu, H. Chen, Rational Construction of Light-Driven Catalysts For CO2 Reduction, Energy Fuels. 35 (7) (2021) 5696–5715, https://doi.org/10.1021/acs.energyfuels.1c00285.
[14] J. Guo, Y. Liang, L. Liu, J. Hu, H. Wang, W. An, W. Cui, Noble-metal-free CdS/Ni-MOF composites with highly efficient charge separation for photocatalytic H2 evolution, Appl. Surf. Sci. 522 (2020), https://doi.org/10.1016/j.apsusc.2020.146356.
[15] L. Niu, T. Wu, M. Chen, L. Yang, Z. Wang, A.A. Kornyshev, H. Jiang, S. Bi, G. Feng, Conductive Metal–Organic Frameworks For Supercapacitors, Adv. Mater. 4 (52) (2022) 2200999, https://doi.org/10.1002/adma.202200999.
[16] H. Gao, H. Shen, H. Wu, H. Jing, Y. Sun, B. Liu, Z. Chen, J. Song, L. Lu, Z. Wu, Q. Hao, Review of Pristine Metal-Organic Frameworks for Supercapacitors: Recent Progress and Perspectives, Energy Fuels. 35 (16) (2021) 12884–12901, https://doi.org/10.1021/acs.energyfuels.1c01722.
[17] M. Xu, X. Wang, K. Ouyang, Z. Xu, Two-dimensional metal-organic framework nanosheets grown on carbon fiber paper interwoven with polyaniline as an electrode for supercapacitors, Energy Fuels. 35 (23) (2021) 19818–19826, https://doi.org/10.1021/acs.energyfuels.1c03170.
[18] R. Hughes, G. Kotamreddy, A. Ostace, D. Bhattacharyya, R. Siegelman, S. T. Parker, S.A. Didas, J.R. Long, B. Omell, M.Matuszewski. Isotherm, Kinetic, process modeling, and techno-economic analysis of a diamine-appended metal-organic framework for CO_2 capture using fixed bed contactors, Energy Fuels. 35 (7) (2021) 6040–6055, https://doi.org/10.1021/acs.energyfuels.0c04359.
[19] A.A. Vodyashkin, A.V. Sergorodceva, P. Kezimana, Y.M. Stanishevskiy, Metal-organic framework (MOF)—A universal material for biomedicine, Int. J. Mol. Sci. 24 (9) (2023) 7819, https://doi.org/10.3390/ijms24097819.
[20] J. Wang, T. Hu, Q. Han, W. Luo, J. Zhong, M. Ding, The synthesis and functionalization of metal organic frameworks and their applications for the

selective separation of proteins/peptides, Anal. Bioanal. Chem. 415 (24) (2023), https://doi.org/10.1007/s00216-023-04843-z.
[21] M. Wang, M. Hu, Z. Li, L. He, Y. Song, Q. Jia, Z. Zhang, M. Du, Construction of Tb-MOF-on-Fe-MOF conjugate as a novel platform for ultrasensitive detection of carbohydrate antigen 125 and living cancer cells, Biosens. Bioelectron. 142 (2019) 111536, https://doi.org/10.1016/j.bios.2019.111536.
[22] X. Wang, Z. Zhang, W. Huang, X. Li, B. Yan, Preparation of highly water stable HKUST-1@Pyr composites for excellent CO_2 capture capability and efficient separation of CO2/N2, Inorg. Chem. Commun. 156 (2023) 111252, https://doi.org/10.1016/j.inoche.2023.111252.
[23] Y. Chen, X. Mu, E. Lester, T. Wu, High efficiency synthesis of HKUST-1 under mild conditions with high BET surface area and CO2 uptake capacity, Progress Nat. Sci.: Mater. Inter. 28 (5) (2018) 584–589, https://doi.org/10.1016/j.pnsc.2018.08.002.
[24] K.S. Lin, A.K. Adhikari, C.N. Ku, C.L. Chiang, H. Kuo, Synthesis and characterization of porous HKUST-1 metal organic frameworks for hydrogen storage, Int. J. Hydrogen. Energy. 37 (18) (2012) 13865–13871, https://doi.org/10.1016/j.ijhydene.2012.04.105.
[25] C. Prestipino, L. Regli, J.G. Vitillo, F. Bonino, A. Damin, C. Lamberti, A. Zecchina, P.L. Solari, K.O. Kongshaug, S. Bordiga, Local structure of framework Cu(II) in HKUST-1 metallorganic framework: Spectroscopic characterization upon activation and interaction with adsorbates, Chem. Mater. 18 (5) (2006) 1337–1346, https://doi.org/10.1021/cm052191g.
[26] R. Aman, A. Clearfield, M. Sadiq, Z. Ali, HKUST-1 Supported on Zirconium Phosphate as an Efficient Catalyst for Solvent Free Oxidation of Cyclohexene: DFT Study, Catalysts 8 (11) (2018) 546, https://doi.org/10.3390/CATAL8110546.
[27] M. Todaro, G. Buscarino, L. Sciortino, A. Alessi, F. Messina, M. Taddei, M. Ranocchiari, M. Cannas, F.M. Gelardi, Decomposition Process of Carboxylate MOF HKUST-1 Unveiled at the Atomic Scale Level, J. Phys. Chem. C. 120 (23) (2016) 12879–12889. doi:10.1021/acs.jpcc.6b03237.
[28] J. Sun, M. Shang, M. Zhang, S. Yu, Z. Yuan, X. Yi, S. Filatov, J. Zhang, Konjac glucomannan/cellulose nanofibers composite aerogel supported HKUST-1 for CO_2 adsorption, Carbohydr. Polym. 293 (2022)119720. doi:10.1016/j.carbpol.2022.119720.
[29] S. Park, J. Ryu, H.Y. Cho, D. Sohn,Halloysite nanotubes loaded with HKUST-1 for CO 2 adsorption, Colloids. Surf. A Physicochem. Eng. Asp. 651 (2022)129750. doi:10.1016/j.colsurfa.2022.129750.
[30] J. Cortés-Súarez, V. Celis-Arias, H.I. Beltrán, A. Tejeda-Cruz, I.A. Ibarra, J.E. Romero-Ibarra, E. Sánchez-González, S. Loera-Serna, Synthesis and Characterization of an SWCNT@HKUST-1 Composite: Enhancing the CO 2 Adsorption Properties of HKUST-1, ACS Omega. 4 (3) (2019) 5275–5282. doi:10.1021/acsomega.9b00330.
[31] F. Xu, Y. Yu, J. Yan, Q, Xia, H. Wang, J. Li, Z. Li,Ultrafast room temperature synthesis of GrO@HKUST-1 composites with high CO2 adsorption capacity and CO2/N2 adsorption selectivity, Chem. Eng. J. 303 (2016) 231–237. doi:10.1016/j.cej.2016.05.143.
[32] N. Al-Janabi, P. Hill, L. Torrente-Murciano, A. Garforth, P. Gorgoja, F. Siperstein, X. Fan, Mapping the Cu-BTC metal-organic framework (HKUST-1) stability envelope in the presence of water vapour for CO2 adsorption from flue gases, Chem. Eng. J. 281 (2015) 669–677. doi:10.1016/j.cej.2015.07.020.
[33] X. Yan, S. Komarneni, Z. Zhang, Z. Yan, Extremely enhanced CO2 uptake by HKUST-1 metal-organic framework via a simple chemical treatment, Microporous Mesoporous Mater 183 (2014) 69–73, https://doi.org/10.1016/j.micromeso.2013.09.009.
[34] S. Ye, X. Jiang, L.-W.Ruan, B. Liu, Y.-M. Wang, J.-F. Zhu, L.-G. Qiu, Post-combustion CO2 capture with the HKUST-1 and MIL-101(Cr) metal-organic frameworks: Adsorption, separation and regeneration investigations, Microporous Mesoporous Mater. 179 (2013) 191–197. doi:10.1016/j.micromeso.2013.06.007.
[35] J. Moellmer, A. Moeller, F. Dreisbach, R. Glaeser, R. Staudt, High pressure adsorption of hydrogen, nitrogen, carbon dioxide and methane on the metal-organic framework HKUST-1, Microporous Mesoporous Mater. 138 (1–3) (2011) 140–148. https://, https://doi.org/10.1016/j.micromeso.2010.09.013.
[36] J. Liu, Y. Wang, A.I. Benin, P. Jakubczak, R.R. Willis, M.D. LeVan, CO2/H2O adsorption equilibrium and rates on metal-organic frameworks: HKUST-1 and Ni/DOBDC, Langmuir 26 (17) (2010) 14301–14307, https://doi.org/10.1021/la102359q.
[37] X. Ma, S. Peng, W. Li, H. Liu, Y. Chen, Efficient Removal of Low Concentration Methyl Mercaptan By HKUST-1 Membrane Constructed On Porous Alumina Granules, Cryst. Eng. Com. 20 (2018) 407–411, https://doi.org/10.1039/C7CE01922J.
[38] Q.M. Wang, D. Shen, M. Bülow, M.L. Lau, S. Deng, F.R. Fitch, N.O Lemcoff, J. Semanscin, Metallo Organic Molecular Sieve For Gas Separation and Purification, Microporous Mesoporous Mater 55 (2) (2002) 217–230, https://doi.org/10.1016/S1387-1811(02)00405-5.
[39] N. Mehio, S. Dai, D.E. Jiang, Quantum mechanical basis for kinetic diameters of small gaseous molecules, J. Phys. Chem. A. 118 (6) (2014) 1150–1154, https://doi.org/10.1021/jp412588f.
[40] T. Ghanbari, F. Abnisa, W.M.A. Wan Daud, A review on production of metal organic frameworks (MOF) for CO_2 adsorption, Sci. Total Environ. 707 (2020) 135090. doi:10.1016/j.scitotenv.2019.135090.
[41] Z. Wang, L. Liu, Z. Li, N. Goyal, T. Du, J. He, G.K. Li, Shaping of Metal-Organic Frameworks: A Review, Energy Fuels 36 (6) (2022) 2927–2944, https://doi.org/10.1021/acs.energyfuels.1c03426.
[42] S. Lawson, M. Snarzyk, D. Hanify, A.A. Rownaghi, F. Rezaei, Development of 3D-Printed Polymer-MOF Monoliths for CO2 Adsorption, Ind. Eng. Chem. Res. 59 (15) (2020) 7151–7160., https://doi.org/10.1021/acs.iecr.9b05445.
[43] H. Thakkar, S. Eastman, Q. Al-Naddaf, A.A. Rownaghi, F. Rezaei, 3D-Printed Metal-Organic Framework Monoliths for Gas Adsorption Processes, ACS. Appl. Mater. Interfaces. 9 (41) (2017) 35908–35916., https://doi.org/10.1021/acsami.7b11626.
[44] G.J.H. Lim, Y. Wu, B.B. Shah, J.J. Koh, C.K. Liu, D. Xhao, A.K. Cheetham, J. Wang, J. Ding, 3D-Printing of Pure Metal-Organic Framework Monoliths, ACS. Mater. Lett. 1 (1) (2019) 147–153, https://doi.org/10.1021/acsmaterialslett.9b0006.
[45] S. Lawson, A.A. Alwakwak, A.A. Rownaghi, F. Rezaei, Gel-Print-Grow: A New Way of 3D Printing Metal-Organic Frameworks, ACS. Appl. Mater. Interfaces. 12 (50) (2020) 56108–56117. doi:10.1021/acsami.0c18720.
[46] H. Thakkar, S. Eastman, A. Hajari, A.A. Rownaghi, J.C. Knox, F. Rezaei, 3D-Printed Zeolite Monoliths for CO_2 Removal from Enclosed Environments, ACS. Appl. Mater. Interfaces. 8 (41) (2016) 27753–27761., https://doi.org/10.1021/acsami.6b09647.
[47] W.W. Lestari, M. Adreane, C. Purnawan, H. Fansuri, N. Widiastuti, S.B. Rahardjo, Solvothermal and electrochemical synthetic method of HKUST-1 and its methane storage capacity, IOP Conf. Ser. Mater. Sci. Eng. 107 (2016) 012030, https://doi.org/10.1088/1757-899X/107/1/012030.
[48] Y. He, Y. Wang, J. Shi, X. Lu, Q. Liu, Y. Liu, T. Zhu, D. Wang, Q. Yang, Incorporating Metal–Organic Frameworks Into Substrates for Environmental Applications, Chem. Eng. J. 446 (2) (2022) 136866, https://doi.org/10.1016/j.cej.2022.136866.
[49] J. Huang, R. Gipson, C. Wang, S.X. Zhang, S. Guddati, S.M.L. Nai, Emerging 3D-printed zeolitic gas adsorbents, Mater. Science Addit. Manuf. 2 (4) (2023) 1880., https://doi.org/10.36922/msam.1880.
[50] P. Küsgens, A. Zgaverdea, H.G. Fritz, S. Siegle, S. Kaskel, Metal-organic frameworks in monolithic structures, J. Am. Ceram. Soc. 93 (9) (2010) 2476–2479., https://doi.org/10.1111/j.1551-2916.2010.03824.x.
[51] Y. Liu, Z. Ng, E.A. Khan, H.K. Jeong, C. bun Ching, Z. Lai, Synthesis of continuous MOF-5 membranes on porous α-alumina substrates, Micropor. Mesopor. Mat. 118 (1–3) (2009) 296–301, https://doi.org/10.1016/j.micromeso.2008.08.054.
[52] M. Arnold, P. Kortunov, D.J. Jones, Y. Nedellec, J. Kärger, J. Caro, Oriented crystallisation on supports and anisotropic mass transport of the metal-organic framework manganese formate, Eur. J. Inorg. Chem. 1 (2007) 60–64., https://doi.org/10.1002/ejic.200600698.
[53] S. Lawson, A. Hajari, A.A. Rownaghi, F. Rezaei, MOF immobilization on the surface of polymer-cordierite composite monoliths through in-situ crystal growth, Sep. Purif. Technol. 183 (2017) 173–180., https://doi.org/10.1016/j.seppur.2017.03.072.
[54] J.J. Torrez-Herrera, S.A. Korili, A. Gil, Development of ceramic-MOF filters from aluminum saline slags for capturing CO2, Powder. Technol. 429 (2023) 118962, https://doi.org/10.1016/j.powtec.2023.118962.
[55] N. Fijoł, A. Mautner, E.S. Grape, Z. Bacsik, A.K. Inge, A.P. Mathew, MOF@Cell: 3D printed biobased filters anchored with a green metal-organic framework for effluent treatment, J. Mater. Chem. a Mater. 11 (23) (2023) 12384–12394., https://doi.org/10.1039/d3ta01757e.
[56] L. Fei, L. Shen, C. Chen, J. Xu, B. Wang, B. Li, H. Lin, Assembling 99% MOFs into Bioinspired Rigid-Flexible Coupled Membrane with Significant Permeability: The Impacts of Defects, Small 20 (2024) 2306528, https://doi.org/10.1002/smll.202306528.
[57] D. Wu, Q. Zhang, R. Gao, Mechanical stability of ZSM-5 zeolite washcoated cordierite monoliths, Chem. Eng. Res. Des. 168 (2021) 426–434., https://doi.org/10.1016/j.cherd.2021.02.026.
[58] W. Guan, Y. Dai, C. Dong, X. Yang, Y. Xi, Zeolite imidazolate framework (ZIF)-based mixed matrix membranes for CO2 separation: A review, J. Appl. Polym. Sci. 137 (33) (2020) 48968, https://doi.org/10.1002/app.48968.
[59] M.C. Bacariza, A.N. Mendes, C. Ozhan, P.Da Costa, C. Henriques, Optimizing Washcoating Conditions for the Preparation of Zeolite-Based Cordierite Monoliths for NOx CH4-SCR: A Required Step for Real Application, Ind. Eng. Chem. Res. 58 (27) (2019) 11799–11810., https://doi.org/10.1021/acs.iecr.9b01216.
[60] Y. Zhang, Q. Su, Z. Wang, Y. Yang, Y. Xin, D. Han, X. Yang, H. Wang, X. Gao, Z. Zhang, Synthesis and toluene adsorption/desorption property of beta zeolite coated on cordierite honeycomb by an in situ crystallization method, Chem. Eng. Technol. 31 (12) (2008) 1856–1862, https://doi.org/10.1002/ceat.200800260.
[61] T. Wang, S. Yang, K. Sun, X. Fang, Preparation of Pt/beta zeolite-Al2O3/cordierite monolith for automobile exhaust purification, Ceram. Int. 37 (2) (2011) 621–626, https://doi.org/10.1016/j.ceramint.2010.09.035.
[62] B. Mitra, D. Kunzru, Washcoating of different zeolites on cordierite monoliths, J. Am. Ceram. Soc. 91 (1) (2008) 64–70., https://doi.org/10.1111/j.1551-2916.2007.02032.x.
[63] L.A. Darunte, C.R.Murdock Y.Terada, K.S. Walton, D. S.Sholl, C.W. Jones, Monolith-Supported Amine-Functionalized Mg2(dobpdc) Adsorbents for CO2 Capture, ACS Appl. Mater. Inter. 9 (20) (2017) 17042–17050., https://doi.org/10.1021/acsami.7b02035.
[64] U. Betke, S. Proemmel, S. Rannabauer, A. Lieb, M. Scheffler, F. Scheffler, Silane functionalized open-celled ceramic foams as support structure in metal organic framework composite materials, Micropor. Mesopor. Mater. 239 (2017) 209–220, https://doi.org/10.1016/j.micromeso.2016.10.011.
[65] U. Betke, M. Klaus, J.G. Eggebrecht, M. Scheffler, A. Lieb, MOFs meet macropores: Dynamic direct crystallization of the microporous aluminum isophthalate CAU-10 on reticulated open-cellular alumina foams, Microp. Mesopor. Mater. 265 (2018) 43–56. doi:10.1016/j.micromeso.2018.01.020.

[66] J. Campbell, B. Tokay, Controlling the size and shape of Mg-MOF-74 crystals to optimise film synthesis on alumina substrates, Micropor. Mesopor. Mat. 251 (2017) 190–199., https://doi.org/10.1016/j.micromeso.2017.05.058.

[67] F. Rezaei, S. Lawson, H. Hosseini, H. Thakkar, A. Hajari, S. Monjezi, A. A. Rownaghi, MOF-74 and UTSA-16 film growth on monolithic structures and their CO2 adsorption performance, Chem. Eng. J. 313 (2017) 1346–1353., https://doi.org/10.1016/j.cej.2016.11.058.

[68] J. Gascon, S. Aguado, F. Kapteijn, Manufacture of dense coatings of Cu3(BTC)2 (HKUST-1) on α-alumina, Micropor. Mesopor. Mater. 113 (1–3) (2008) 132–138, https://doi.org/10.1016/j.micromeso.2007.11.014.

[69] T. Granato, F. Testa, R. Olivo, Catalytic activity of HKUST-1 coated on ceramic foam, Micropor. Mesopor. Mater. 153 (2012) 236–246., https://doi.org/10.1016/j.micromeso.2011.12.055.

[70] Y. Chen, N. Wang, O. Ola, Y. Xia, Y. Zhu, Porous ceramics: Light in weight but heavy in energy and environment technologies, Mater. Sci. Eng. R Rep.143 (2021) 100589. doi:10.1016/j.mser.2020.100589.

[71] M.F. Ashby, The properties of foams and lattices, Philos. Trans. A. Math. Phys. Eng. Sci. 364 1838 (2006) 15–30., https://doi.org/10.1098/rsta.2005.1678.

[72] J. Feng, J. Fu, X. Yao, Y. He, Triply Periodic Minimal Surface (TPMS) Porous structures: From multi-Scale design, Precise Additive Manufacturing to Multidisciplinary Applications, Int. J. Extrem Manuf. 4 (2022) 022001. doi:10.1088/2631-7990/ac5be6.

[73] L. Zhang, Z. Hu, M.Y. Wang, S. Feih, Hierarchical sheet triply periodic minimal surface lattices: Design, geometric and mechanical performance, Mater. Des. 209 (2021) 109931. doi:10.1016/j.matdes.2021.109931.

[74] J. Lu, P. Dong, Y. Zhao, Y. Zhao, Y. Zeng, 3D printing of TPMS structural ZnO ceramics with good mechanical properties, Ceram. Int. 47 (9) (2021) 12897–12905., https://doi.org/10.1016/j.ceramint.2021.01.152.

[75] P. Karimipour-Fard, A.H. Behravesh, H. Jones-Taggart, R. Pop-Iliev, G. Rizvi, Effects of design, porosity and biodegradation on mechanical and morphological properties of additive-manufactured triply periodic minimal surface scaffolds, J. Mech. Behav. Biomed. Mater. 112 (2020) 104064, https://doi.org/10.1016/j.jmbbm.2020.104064.

[76] S. Vijayavenkataraman, L.Y. Kuan, W.F. Lu, 3D-printed ceramic triply periodic minimal surface structures for design of functionally graded bone implants, Mater. Des. 191 (2020) 108602, https://doi.org/10.1016/j.matdes.2020.108602.

[77] C. Pan, Y. Han, J. Lu, Design and Optimization of Lattice structures: A review, Appl. Sci. 10 (18)(2020) 6374. doi:10.3390/app10186374.

[78] S. Sobhani, S. Allan, P. Muhunthan, E. Boigne, M. Ihme, Additive Manufacturing of Tailored Macroporous Ceramic Structures for High-Temperature Applications, Adv. Eng. Mater. 22 (8) (2020) 2070035, https://doi.org/10.1002/adem.202070035.

[79] S. Yu, J. Sun, J. Bai, Investigation of functionally graded TPMS structures fabricated by additive manufacturing, Mater. Des. 182 (2019) 108021, https://doi.org/10.1016/j.matdes.2019.108021.

[80] O. Al-Ketan, R.K. Abu Al-Rub, Multifunctional Mechanical Metamaterials Based on Triply Periodic Minimal Surface, Lattices 21 (10) (2019) 1900524, https://doi.org/10.1002/adem.201900524.

[81] J.Y. Huang, H. Xu, E. Peretz, D.Y. Wu, C.K. Ober, T. Hanrath, Three-Dimensional Printing of Hierarchical Porous Architectures, Chem. Mater. 31 (24) (2019) 10017–10022., https://doi.org/10.1021/acs.chemmater.9b02761.

[82] Y. Lakhdar, C. Tuck, J. Binner, A. Terry, R. Goodridge, Additive Manufacturing of Advanced Ceramic Materials,, Prog. Mater. Sci. (2021) 100736, https://doi.org/10.1016/j.pmatsci.2020.100736.

[83] N. Travitzky, A. Bonet, B. Dermeik, T. Fey, I. Filbert-Demut, L. Schlier, T. Schlordt, P. Greil, Additive manufacturing of ceramic-based materials, Adv. Eng. Mater.16 6 (2014) 729–754, https://doi.org/10.1002/adem.201400097.

[84] A. Zocca, P. Colombo, C.M. Gomes, J. Günster, Additive Manufacturing of Ceramics: Issues, Potentialities, and Opportunities, J. Am. Ceram. Soc. 98 (7) (2015) 1983–2001, https://doi.org/10.1111/jace.13700.

[85] J. Stampfl, M. Schwentenwein, J. Homa, F.B. Prinz, Lithography-based additive manufacturing of ceramics: Materials, applications and perspectives, MRS Commun. 13 (5) (2023) 786–794., https://doi.org/10.1557/s43579-023-00444-0.

[86] T. Lube, M. Staudacher, A.K. Hofer, J. Schlacher, R. Bermejo, Stereolithographic 3D Printing of Ceramics: Challenges and Opportunities for Structural Integrity, 25 (7)(2023) 2200520. doi:10.1002/adem.202200520.

[87] S. Mamatha, P. Biswas, R. Johnson, Digital Light Processing of ceramics: an Overview On process, Materials and Challenges, Prog. Addit. Manuf.8 (2023) 1083–1102, https://doi.org/10.1007/s40964-022-00379-3.

[88] S.A. Rasaki, D. Xiong, S. Xiong, F. Su, M. Idrees, Z. Chen, Photopolymerization-based Additive Manufacturing of ceramics: A systematic Review, J. Adv. Ceram. 10 (2021) 442–471, https://doi.org/10.1007/s40145-021-0468-z.

[89] S.N. Sluijter, J. Boon, J. James, S. Krishnamurthy, A. Lind, R. Blom, K. A. Andreassen, A.M. Cormos, V.C. Sandu, R. de Boer, 3D-printing of adsorbents for increased productivity in carbon capture applications (3D-CAPS), Int. J. Greenh. Gas Control 112 (2021) 103512, https://doi.org/10.1016/j.ijggc.2021.103512.

[90] L.K.S. Lima, K.R. Silva, R.R. Menezes, L.N.L. Santana, H.L. Lira, Microstructural characteristics, properties, synthesis and applications of mullite: a review, Ceram 68 (385) (2022) 126–142, https://doi.org/10.1590/0366-69132022683853184.

[91] R. Salomão, L. Fernandes, N.C.M. Spera, Combined effects of SiO2 ratio and purity on physical properties and microstructure of in situ alumina-mullite ceramic, Int. J. Appl. Ceram. Technol. 18 (5) (2021) 1702–1709., https://doi.org/10.1111/ijac.13733.

[92] H. Schneider, R.X. Fischer, J. Schreuer, Mullite: Crystal Structure and Related Properties, J. Am. Ceram. Soc. 98 (10) (2015) 2948–2967. doi:10.1111/jace.13817.

[93] B. Saruhan, W. Albers, H. Schneider, W.A. Kaysser, Reaction and Sintering Mechanisms of Mullite in the Systems Cristobalite/a-Al2O3 and Amorphous SiO2/a-Al2O3, J. Eur. Ceram. Soc. 16 (10) (1996) 1075–1081, https://doi.org/10.1016/0955-2219(96)00023-4.

[94] I.L. de Camargo, R. Erbereli, J.F.P. Lovo, R. Fortulan, C.A. Fortulan, Digital light processing additive manufacturing of in situ mullite-zirconia composites, J. Eur. Ceram. Soc. 42 (13) (2022) 6025–6032., https://doi.org/10.1016/j.jeurceramsoc.2022.06.042.

[95] I.L. de Camargo, R. Erbereli, C.A. Fortulan, Additive manufacturing of electrofused mullite slurry by digital light processing, J. Eur. Ceram. Soc. 41 (14) (2021) 7182–7188., https://doi.org/10.1016/j.jeurceramsoc.2021.07.005.

[96] C. He, X. Liu, C. Ma, X. Li, F. Hou, L. Yan, A. Guo, J. Liu, Digital light processing fabrication of mullite component derived from preceramic precusor using photosensitive hydroxysiloxane as the matrix and alumina nanoparticles as the filler, J. Eur. Ceram. Soc. 41 (11) (2021) 5570–5577, https://doi.org/10.1016/j.jeurceramsoc.2021.04.051.

[97] J. Schmidt, A.A. Altun, M. Schwentenwein, P. Colombo, Complex mullite structures fabricated via digital light processing of a preceramic polysiloxane with active alumina fillers, J. Eur. Ceram. Soc. 39 (4) (2019) 1336–1343, https://doi.org/10.1016/j.jeurceramsoc.2018.11.038.

[98] R.T. Lee, W.S. Cheng, C.S. Lee, F.F. Lin, F.H. Liu, Mullite ceramic fabrication by 3D printing, in: J.F. Silva Gomes, S.A. Meguid (Eds.), Proc. 7th Int. Conf. Mech. Mater. Des., Albufeira, Portugal 11-15 June 2017, 2017, pp. 779–784.

[99] Y. Milovanov, A. Bertero, B. Coppola, P. Palmero, J.M. Tulliani, Mullite 3D Printed Humidity Sensors, Ceram. 7 (2) (2024) 807–820, https://doi.org/10.3390/ceramics7020053.

[100] L. Montanaro, J.M. Tulliani, C. Perrot, A. Negro, Sintering of Industrial Mullites, J. Eur. Ceram. Soc. 11 (14) (1997) 1715–1723, https://doi.org/10.1016/s0955-2219(97)00043-5.

[101] V. Crivianu-Gaita, A. Romaschin, M. Thompson, High efficiency reduction capability for the formation of Fab' antibody fragments from F(ab)2 units, Biochem. Biophys. Rep. 2 (2015) 23–28, https://doi.org/10.1016/j.bbrep.2015.04.004.

[102] W.Y. Gao, K. Leng, L. Cash, M. Chrzanowski, C.A. Stackhouse, Y. Sun, S. Ma, Investigation of prototypal MOFs consisting of polyhedral cages with accessible Lewis-acid sites for quinoline synthesis, Chem. Commun. 51 (23) (2015) 4827–4829, https://doi.org/10.1039/C4CC09410G.

[103] M. Hartmann, S. Kunz, D. Himsl, O. Tangermann, S. Ernst, A. Wagener, Adsorptive separation of isobutene and isobutane on Cu3(BTC) 2, Langmuir 24 (16) (2008) 8634–8642, https://doi.org/10.1021/la8008656.

[104] K. Schlichte, T. Kratzke, S. Kaskel, Improved synthesis, thermal stability and catalytic properties of the metal-organic framework compound Cu3(BTC)2, Microporous and Mesoporous, Materials 73 (1–2) (2004) 81–88, https://doi.org/10.1016/J.MICROMESO.2003.12.027.

[105] Z. Ni, R.I. Masel, Rapid production of metal-organic frameworks via microwave-assisted solvothermal synthesis, J. Am. Chem. Soc. 128 (38) (2006) 12394–12395. doi:10.1021/ja0635231.

[106] A. Domán, O. Czakkel, L. Porcar, J. Madarász, E. Geissler, K. László, Role of water molecules in the decomposition of HKUST-1: Evidence from adsorption, thermoanalytical, X-ray and neutron scattering measurements, Appl. Surf. Sci. 480 (2019) 138–147, https://doi.org/10.1016/j.apsusc.2019.02.177.

[107] M. Thommes, K. Kaneko, A.V. Neimark, J.P. Olivier, F. Rodriguez-Reinoso, J. Rouquerol, K.S.W. Sing, Physisorption of gases, with special reference to the evaluation of surface area and pore size distribution (IUPAC Technical Report), Pure Appl. Chem. 87 (9–10) (2015) 1051–1069, https://doi.org/10.1515/pac-2014-1117.

[108] P. Jagódka, K. Matus, A. Łamacz, On the HKUST-1/GO and HKUST-1/rGO Composites: The Impact of Synthesis Method on Physicochemical Properties, Molecules 27 (20) (2022) 7082, https://doi.org/10.3390/molecules27207082.

[109] I.L. de Camargo, M.M. Morais, C.A. Fortulan, M.C. Branciforti, A review on the rheological behavior and formulations of ceramic suspensions for vat photopolymerization, Ceram. Int. 47 (9) (2021) 11906–11921, https://doi.org/10.1016/j.ceramint.2021.01.031.

[110] R.P. Chhabra, J.F. Richardson,Non-Newtonian fluid behaviour in: R.P. Chhabra, J.F. Richardson (Eds.) Non-Newtonian Flow and Applied rheology. Butterworth Heinemann, Oxford, 2008, pp. 1–55. doi:10.1016/B978-0-7506-8532-0.X0001-7.

[111] Y. Wu, A. Kobayashi, G.J. Halder, V.K. Peterson, K.W. Chapman, N. Lock, P. D. Southon, C.J. Kepert, Negative thermal expansion in the metal-organic framework material Cu 3(1,3,5-benzenetricarboxylate)2, Angew. Chem. Int. Edit. 47 (46) (2008) 8929–8932, https://doi.org/10.1002/anie.200803925.

[112] J.S. Moya, C. Baudín, P. Miranzo, Sintering, in: R.A. Meyers (Ed.), Encyclopedia of Physical Science and Technology, Academic Press, USA, 2003, pp. 865–878, https://doi.org/10.1016/B0-12-227410-5/00694-3.

[113] Z. Wang, P.G. Weidler, C. Azucena, L. Heinke, C. Wöll, Negative, anisotropic thermal expansion in monolithic thin films of crystalline metal-organic frameworks, Micropor. Mesopor. Mat. 222 (2016) 241–246, https://doi.org/10.1016/j.micromeso.2015.10.016.

[114] V. Papetti, P. Dimopoulos Eggenschwiler, A. Della Torre, F. Lucci, A. Ortona, G. Montenegro, Additive Manufactured open cell polyhedral structures as substrates for automotive catalysts, Int. J. Heat. Mass Transf. 126 (2018) 1035–1047, https://doi.org/10.1016/j.ijheatmasstransfer.2018.06.061.

[115] Y. Man, G. Ding, L. Xudong, K. Xue, D. Qu, Z. Xie, A Review On Porous Ceramics With Hierarchical Pore Structure By 3D Printing-Based Combined Route, J. Asian

Ceram. Soc. 9 (4) (2021) 1377–1389, https://doi.org/10.1080/21870764.2021.1981571.

[116] S. Kartohardjono, K. Alexander, A. Larasati, I.C. Sihombing, Effect of Feed Gas Flow Rate on CO2 Absorption through Super Hydrophobic Hollow Fiber membrane Contactor, IOP Conf. Ser.: Mater. Sci. Eng. 316 (2018) 012012, https://doi.org/10.1088/1757-899X/316/1/012012.

[117] Y. Liu, S. Liu, A.A.S. Gonçalves, M. Jaroniec, Effect of metal-ligand ratio on the CO_2 adsorption properties of Cu-BTC metal-organic frameworks, RSC Adv 8 (62) (2018) 35551–35556, https://doi.org/10.1039/c8ra07774f.

[118] S. Ye, X. Jiang, L.-W. Ruan, B. Liu, Y.-M. Wang, J.F. Zhu, L.-G. Qiu, Post-combustion CO2 capture with the HKUST-1 and MIL-101(Cr) metal-organic frameworks: Adsorption, separation and regeneration investigations, Micropor. Mesopor. Mat. 179 (2013) 191–197, https://doi.org/10.1016/j.micromeso.2013.06.007.

[119] S. Park, J. Ryu, H.Y. Cho, D. Sohn, Halloysite nanotubes loaded with HKUST-1 for CO2 adsorption, Colloids. Surface A. 651 (2022) 129750. doi:10.1016/j.colsurfa.2022.129750.

[120] F. Xu, Y. Yu, J. Yan, Q. Xia, H. Wang, J. Li, Z. Li, Ultrafast room temperature synthesis of GrO@HKUST-1 composites with high CO2 adsorption capacity and CO2/N2 adsorption selectivity, Chemical Engineering Journal 303 (2016) 231–237, https://doi.org/10.1016/j.cej.2016.05.143.

[121] L.F.A.S. Zafanelli, A. Henrique, H. Steldinger, J.L. Diaz de Tuesta, J. Gläsel, A. E. Rodrigues, H.T. Gomes, B.J.M. Etzold, J.A.C. Silva, 3D-printed Activated Carbon For Post-Combustion CO2 Capture, Micropor. Macropor. Mat. 335 (2022) 111818, https://doi.org/10.1016/j.micromeso.2022.111818.